

Photothermally Modulatable and Structurally Disintegratable Sub-8-nm Au₁Ag₉ Embedded Nanoblocks for Combination Cancer Therapy Produced by Plug-in Assembly

Kishwor Poudel,[#] Sungjae Park,[#] Jungho Hwang,^{*} Sae Kwang Ku, Chul Soon Yong, Jong Oh Kim,^{*} and Jeong Hoon Byeon^{*}



Cite This: *ACS Nano* 2020, 14, 11040–11054



Read Online

ACCESS |



Metrics & More



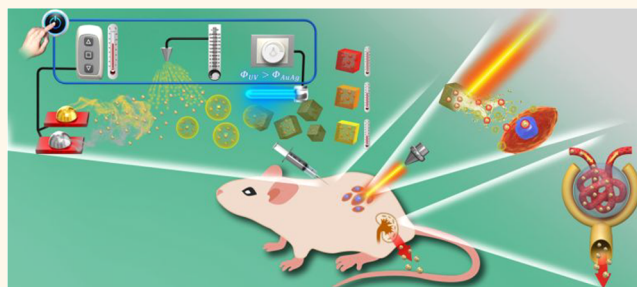
Article Recommendations



Supporting Information

ABSTRACT: As well as the exploration of translatable delivery nanosystems for cancer therapeutic agents, the development of automatable continuous-flow manufacturing technology comprising digitally controlled reactions for the on-demand production of pharmaceuticals is an important challenge in anticancer nanomedicine. Most attempts to resolve these issues have involved the development of alternative reactions, formulations, or constructs containing stimulus components aimed at producing multiple approaches for highly efficacious combination cancer therapies. However, there has been no report of a platform based on plug-in execution that enables continuous-flow manufacture in a compact, reconfigurable manner, although an optimal platform technology may be a prerequisite for the timely translation of recently developed nanomedicines. To this end, we describe the development of a platform toward digitizable, continuous manufacture by a serial combination of plug-in reactionwares (heating plates, a spraying cup, and a photochamber) for single-pass flow fabrication. Specifically, we fabricated three different composite nanoblocks consisting of Au₁Ag₉ (<8 nm; stimulus component), docetaxel (an anticancer drug), and bovine serum albumin (a protective and targeting agent) using our system, with the result of producing nanoblocks with photothermally modulatable and structurally disintegratable properties. These were examined for effectiveness in near-infrared-induced chemothermal cancer therapy and renal excretion of Au₁Ag₉ particles and exhibited high anticancer efficacy and warrantable biosafety.

KEYWORDS: continuous-flow manufacturing, plug-in reactionwares, composite nanoblocks, photothermally modulatable, structurally disintegratable



Although nanoscale silver (Ag) constructs generally exhibit greater plasmonic properties than similarly sized, shaped, or structured gold (Au) counterparts, they are not widely used in biomedical applications because of their chemical instability and potent toxicity due to rapid oxidation, which results in excessive release of Ag ions into tissues and cellular compartments.^{1,2} These issues drove extensive research into the modification of Ag nanoparticles (NPs) by surface or crystal engineering with robust metals or biocompatible organic compounds.^{3–6}

Incorporating Au into the Ag matrix has widely been considered an inorganic modification to overcome the limitations of Ag; AuAg NP composites exhibit different plasmonic properties compared to individual Ag or Au NPs and also reduce the toxicity of Ag by suppressing rapid

oxidation.^{7,8} Modulating the ratio of Au to Ag and the arrangement or shape of Au and Ag atoms can result in different plasmonic properties and biological impacts.^{9,10} Surface modification of Ag NPs using biocompatible compounds (e.g., polymers or proteins) is another strategy for preventing the excessive or off-target release of Ag ions and targeting Ag NPs to cellular compartments.¹¹ This approach has also been used to passivate AuAg NP composites because

Received: December 11, 2019

Accepted: August 20, 2020

Published: August 20, 2020



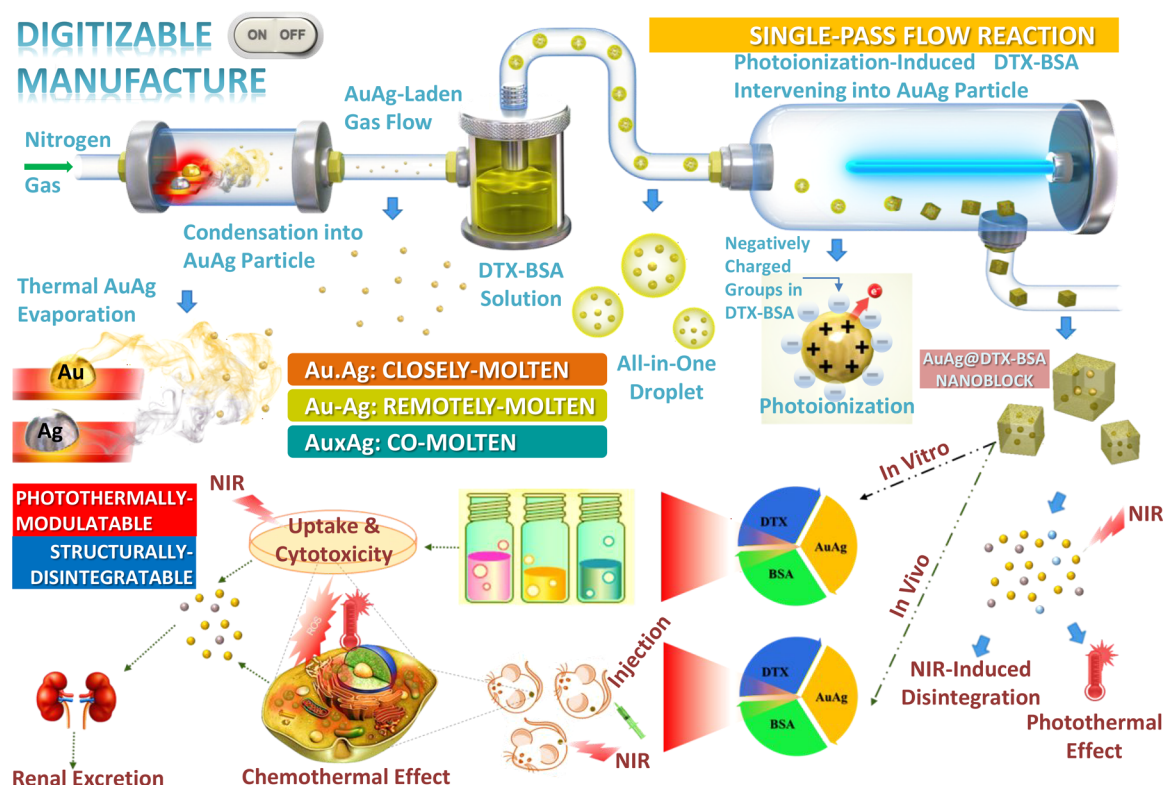


Figure 1. Schematic of the plug-in manufacture system used to fabricate $\text{Au}_1\text{Ag}_9\text{@DTX-BSA}$ NBs consisting of a heating plate, spraying cup, and photochamber and assessment of anticancer efficacy and biosafety. Three different Au_1Ag_9 particles were produced through evaporation–condensation on the heating plates under ambient nitrogen gas flow by changing the arrangement of Au and Ag disks to ensure photothermally modulatable functions. The particle-laden flow was used as the operating fluid for spraying a DTX–BSA solution to produce Au_1Ag_9 particles incorporated into the sprayed droplets as all-in-one precursors. These precursor droplets were eventually exposed to 185 nm UV to positively charge the Au_1Ag_9 particles to induce electrostatic combination with negatively charged groups in the DTX–BSA molecules, resulting in the formation of $\text{Au}_1\text{Ag}_9\text{@DTX-BSA}$ NBs after solvent extraction. The resulting NBs were tested for chemothermal anticancer activity and biosafety in both *in vitro* and *in vivo* models to assess the combination therapeutic efficacy and biosafety. NIR-induced disintegration of the NBs was assessed to evaluate the potential renal excretion and clearance of NBs from the body.

protruding Ag in the composites means that they are still too unstable for dissolution in biological media.^{12–15}

With regard to material processing, the aforementioned modifications have been considered as universal protocols where hydrothermal reactions are manually performed.¹⁶ A toxic surfactant such as cetrimonium bromide is frequently used to functionalize NP surfaces for modification and eventual fabrication of various NP structures with desired physicochemical properties.^{17–21} Moreover, loading NPs with therapeutic agents for combination therapies complicates the processes by requiring additional reactions, steps of separation and purification, and controls.^{22–25} Thus, digitizable or automatable platforms able to manufacture therapeutic or biofunctional materials with modifiable structures and functions are required.^{26–28} To resolve this mismatch between material functions and process complexity, digitized or automated unit operations need to be developed to execute continuous-flow reactions based on plug-in configurations.²⁹

Regarding the issues of cost of Au and retainment of the plasmonic peculiarity of Ag, reducing the proportion of Au in AuAg NP composites has been trialed recently.³⁰ A previous study reported that a Ag-dominant NP composite ($\text{Au}_1\text{Ag}_{2.4}$) was rendered negligibly toxic toward human hepatocytes and kidney cells following surface PEGylation, while the desired plasmonic functions of the composite were retained.³¹ Another study attempted to prepare more Ag-dominant AuAg

composites; however, no meaningful insights relating to biomedical applications were discovered.³² Ensuring optimal ratios of Au to Ag requires manual matrix tests to be performed by expert chemists and involves high costs and effort to validate the efficacy and biosafety of candidate compositions, obstructing the realization of a AuAg composite for clinical application.³³

We have developed a robust plug-in platform for the reconfigurable manufacture of chemothermal therapeutic composite nanosystems by single-pass reaction. Our platform involves serial combination of electrically operated reaction-ware (heating plates, a spraying cup, and a photochamber; Figures 1 and S1A) under ambient nitrogen gas flow to influence the photothermal properties of AuAg particles according to modulatable evaporation–condensation of Au and Ag disks. Because of the simple construction, the heating plates are convenient to operate and easier than laser ablation³⁴ for evaporating Au and Ag vapors from disks with different arrangements (closely $[\text{Au-Ag}]$, remotely $[\text{Au-Ag}]$, and co $[\text{AuxAg}]$ molten; Figure S1B) and ensure different microstructures of AuAg particles from the same proportions of Au and Ag atoms (Au_1Ag_9). Controlling only the surface temperature of the heaters and flow rate of the nitrogen gas enables continuous generation of sub-8-nm Au_1Ag_9 (exhibiting an effective NIR-induced temperature elevation at the minimal input of Au) particles without the use of multiple hydrothermal

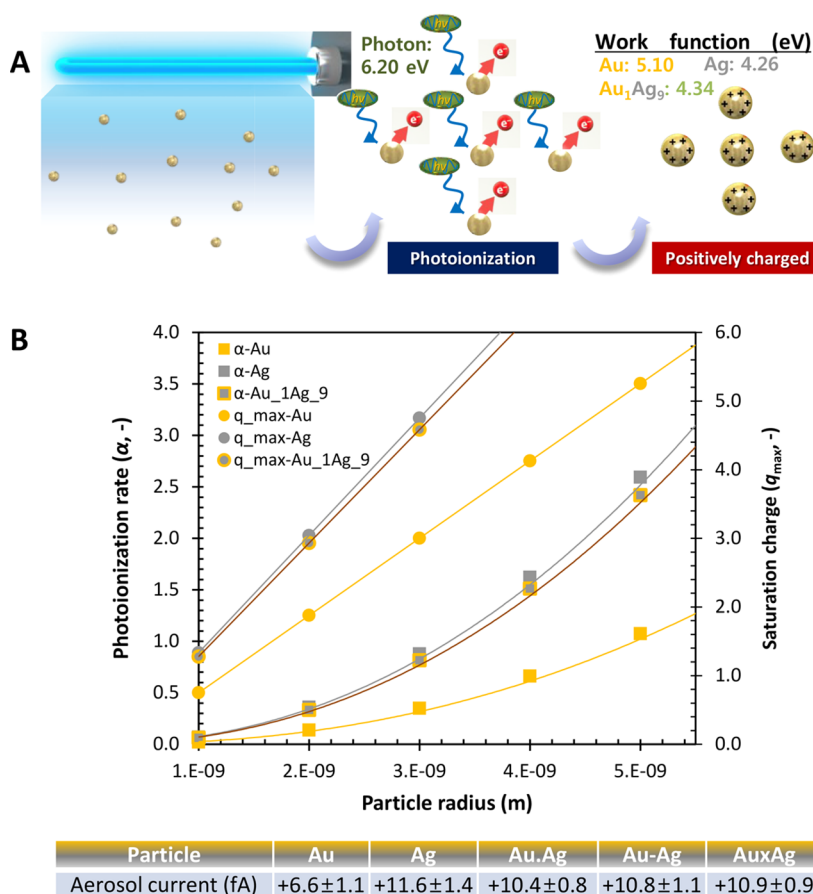


Figure 2. Illustration of the in-flight photoionization of Au₁Ag₉ particles. (A) Schematic model of photoionization of Au₁Ag₉ particles under 185 nm UV irradiation. Electrons on the surface of particles can be detached through attack by photons (6.2 eV, which is greater than the work function of Au₁Ag₉ particles) generated by irradiation, resulting in positive charges on the particle surfaces. (B) Graph of the theoretical photoionization rate (α) and saturation positive charge (q_{\max}) of the irradiated Au₁Ag₉ particles after passing through the photochamber, including Au and Ag particles for comparison. The bottom table shows the aerosol current values of particles produced from closely, remotely, and co-molten disks (Au·Ag, Au-Ag, and AuxAg particles, respectively) as well as Au and Ag particles, representing positive charges on the particles.

reactions and surfactants. This particle-laden flow then passes through the spraying cup and photochamber for successive incorporation and binding with docetaxel (DTX)–bovine serum albumin (BSA) compounds to build composite structures. The BSA is included to maximize the functions of Au₁Ag₉ particles, and DTX confers biocompatibility, versatile surface chemistry, colloidal stability, cost effectiveness, anticancer activities, and blood circulation for the enhanced permeability and retention (EPR) effect.^{35–39} To address the conflicting sizes required for the EPR effect (approximately 50–200 nm for enhanced therapeutic efficacy) and timely renal excretion of cancer therapeutic nanosystems (approximately <8 nm for biosafety),^{40–45} the operating conditions of the spraying cup (orifice diameter and pressure) and photochamber (irradiation intensity and exposure time) were optimized to prepare disintegratable nanoblocks (NBs, ~70 nm) consisting of sub-8 nm Au₁Ag₉ particles and DTX–BSA compounds for low toxicity upon NIR irradiation owing to their thermal collapsing behavior.^{46–49} Three different Au₁Ag₉ particles were incorporated into DTX–BSA compounds by modulating the disk arrangement under 185 nm UV irradiation to configure Au·Ag@DTX–BSA, Au–Ag@DTX–BSA, and AuxAg@DTX–BSA for evaluation of the NBs' photothermal transduction properties. Higher work function (6.2 eV vs

Au₁Ag₉ [4.34 eV]) of the photons generated by irradiation was sufficient to detach electrons from the surfaces of the Au₁Ag₉ particles, creating positively charged particles to which negatively charged groups of the peripheral BSA can interact electrostatically to form Au₁Ag₉@DTX–BSA NBs after in-flight solvent extraction *via* the diffusion dryer.⁵⁰ The resulting NBs were evaluated *in vitro* (MDA-MB-231 cells) and *in vivo* (MDA-MB-231 xenograft tumor-bearing BALB/C nude mice) models to examine the efficacy of chemothermal cancer therapy, as well as renal excretion in the presence of NIR irradiation in relation to the photothermally modulatable and structurally disintegratable configuration.

RESULTS AND DISCUSSION

We evaluated the generation of positive charges on Au₁Ag₉ particles for electrostatic conjugation with BSA by analyzing the photoionization rate (α) and saturation charge (q_{\max}) of particles.⁵¹ Charge currents of Au·Ag, Au–Ag, and AuxAg particles were experimentally obtained using an aerosol electrometer. The photons produced following 185 nm UV irradiation exhibit a greater work function (6.20 eV) than those of Au (5.10 eV), Ag (4.26 eV), or Au₁Ag₉ (4.34 eV) particles, implying that photon exposure can induce electron ejection and generate positive charges on the particle surfaces (Figure

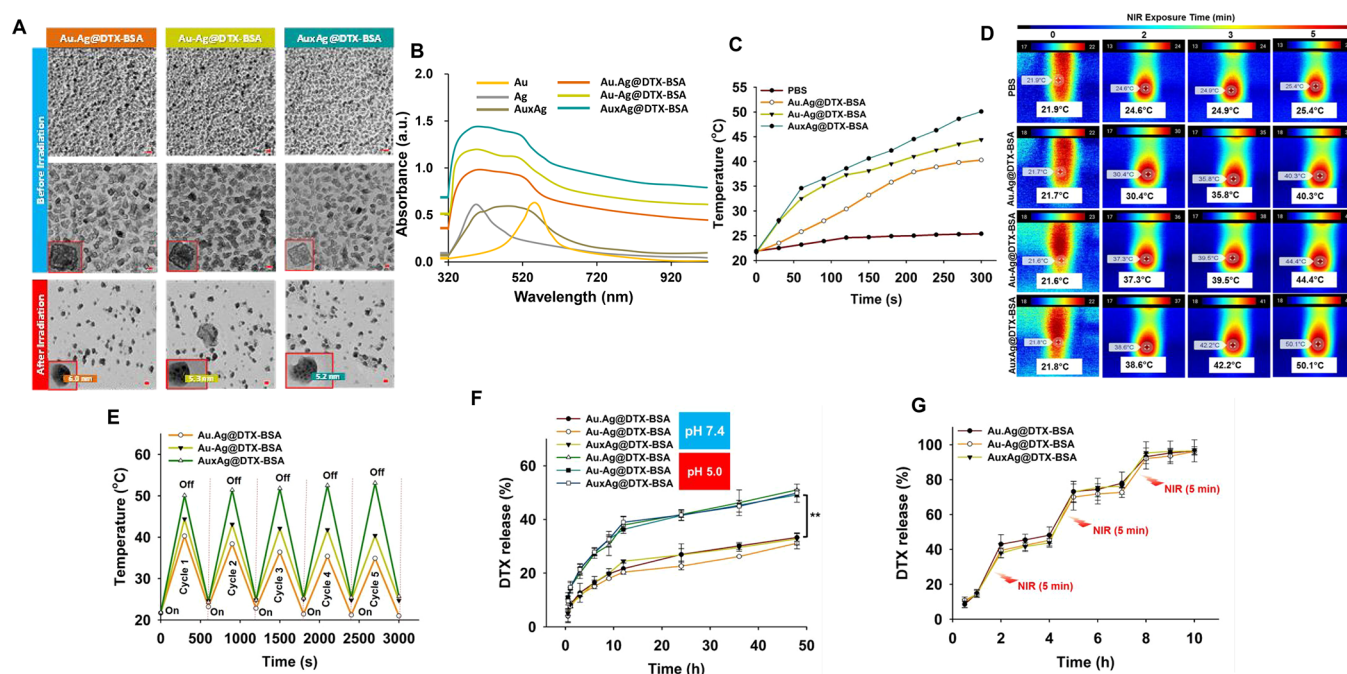


Figure 3. Morphologies, photothermal activities, and the pH- and NIR-responsive DTX release profiles of Au₁Ag₉@DTX-BSA NBs. (A) Low (scale bars, 200 nm)- and high (scale bars, 100 nm)-magnification TEM images of particles produced from closely, remotely, and co-molten disks (Au-Ag, Au-Ag, and AuxAg particles, respectively) incorporated into DTX-BSA droplets (Au-Ag@DTX-BSA, Au-Ag@DTX-BSA, and AuxAg@DTX-BSA NBs, respectively) with or without (scale bars, 50 nm) NIR irradiation. Irradiation with NIR was performed to examine the photothermally disintegratable properties owing to thermal collapse of the three different NBs. (B) UV-vis spectra of the three different NBs, as well as Au, Ag, and AuxAg particles for comparison (0.5 mg/mL, $N = 6$). The starting levels of the profiles were adjusted to avoid overlapping profiles for clarity. (C, D) Time profiles and contours of NIR-induced temperature elevation for the three different NBs indicating the photothermally modulatable function of plug-in manufacture ($N = 6$). (E) Five NIR (808 nm, 2 W/cm²) on (300 s)–off (300 s) cycles were used to evaluate the photothermal conversion stability of the three different NBs. (F, G) pH (5.0 and 7.4)- and NIR (808 nm, 2 W/cm² at pH 5.0)-responsive release profiles of DTX from the three different NBs (for 5 min, $N = 6$).

2A). The imbalance between Au and Ag atoms in the AuAg configuration increased the sensitivity to photon exposures, resulting in greater α and q_{\max} (comparable with Ag particles) than Au particles (Figure 2B). Direct measurement of the electric current of UV-exposed particles (size classified as 6 nm using a nanodifferential mobility analyzer [NDMA]) revealed positive values that differed according to size (inset table of Figure 2B). These values represent electron ejection and match the order of α and q_{\max} (Ag > Au₁Ag₉ > Au). Current levels of Au₁Ag₉ particles were comparable with those of Ag particles, which increased the binding of Au₁Ag₉ particles to negatively charged groups compared with Au particles. Electrostatic interactions between the Au₁Ag₉ particles and DTX-BSA droplets were examined by comparing size distributions of particles, as measured with a scanning mobility particle sizer (SMPS), in the absence and presence of DTX-BSA droplets prior to solvent extraction, as shown in Figure S2. There were no satellite peaks after incorporation into the droplets under 185 nm UV irradiation, despite the more intense peaks of the particles observed before incorporation. This implies that the particles remain within all-in-one droplets upon incorporation. The unimodal size distribution may persist due to electrostatic binding between positively charged particles and negatively charged disulfides of BSA.⁵² Entrapment of DTX in BSA *via* electrostatic and hydrophobic interactions may prevent segregation of DTX molecules from the all-in-one droplets,⁵³ resulting in the unimodal distributions that were observed.

To observe the assembled morphologies of AuAg particles and DTX-BSA droplets, the resulting particles were passed

through a diffusion dryer to extract solvent and directly collected on carbon-coated copper grids in the aerosol state for examination by transmission electron microscopy (TEM). Figure 3A shows low- and high-magnification TEM images of Au-Ag@DTX-BSA, Au-Ag@DTX-BSA, and AuxAg@DTX-BSA. There were no notable differences in distribution between the resulting particles from low-magnification images; high-magnification ones (insets) exhibited block-like shapes regardless of the AuAg particle configuration. The block-like shape may be driven by electrostatic interactions between AuAg particles and DTX-BSA molecules under 185 nm UV irradiation and subsequent stiffening of DTX-BSA of Au-Ag@DTX-BSA, Au-Ag@DTX-BSA, and AuxAg@DTX-BSA NBs from passage through the dryer. Size measurements of hundreds of particles from TEM images revealed the average lateral dimensions of Au-Ag@DTX-BSA, Au-Ag@DTX-BSA, and AuxAg@DTX-BSA NBs to be approximately 60, 75, and 69 nm, respectively. The differences in NB size might result from differences in the photoionization state of Au-Ag, Au-Ag, and AuxAg particles; nevertheless, the sizes of resulting NBs were appropriate for passive targeting to tumors *via* the EPR effect due to leaky and loosely formed junctions in blood vessels and nonspecific adsorptive endocytosis.⁵⁴ The NBs also exhibited differences in contrast; bright regions represented stiffened DTX-BSA molecules, while darker dots indicated AuAg particles embedded in the DTX-BSA matrix (refer to Figure S3). The lattice spacings of Au-Ag, Au-Ag, and AuxAg particles were observed as 0.235, 0.232 (pure Au), 0.228 (pure Ag), and 0.230 nm, respectively, which matched

the (111) planes of incompletely alloyed AuAg, individual Au and Ag, and alloyed AuAg, respectively.^{55–57} The closely molten Au and Ag generated larger (111) spacing (*i.e.*, were less dense) than AuAg, probably due to perturbation by nitrogen gas flow during coevaporation and condensation of Au and Ag, whereas other evaporation configurations adapted to match the known lattice spacings. The ratio of Au to Ag atoms in AuAg particles was determined using scanning electron microscopy–energy dispersive X-ray spectroscopy (SEM–EDS) after the AuxAg particles were sintered to secure a uniform distribution of Au and Ag. This was carried out to ensure measurement accuracy because of their small sizes (Figure S4A). By applying a plate temperature of 1336 °C to Au (which has a melting point of 1064.2 °C) and Ag (961.8 °C) disks, a ratio of 1:9 was achieved using the plug-in system, which was also achieved for Au–Ag and Au–Ag particles. This suggests that the system can modulate the microstructure of AuAg particles in conditions of consistent Au:Ag ratios. This imbalance between the Au and Ag was further observed in the elemental mapping for the part of an AuxAg@DTX–BSA NB (Figure S4B). In X-ray photoelectron spectroscopy (XPS; Figure S5), the separated spin–orbit components of Au (Δ_{Au}) and Ag (Δ_{Ag}) in Au–Ag, Au–Ag, and AuxAg particles were 3.7 and 6.0 eV before combining with DTX–BSA, respectively.⁵⁸ These values match the standard values of Au and Ag and are consistent with the ratio (1:9) of Au to Ag determined using EDS, thus validating the use of heating plates to generate different Au₁Ag₉ particles with identical valence states and compositions. Exposure of Au₁Ag₉ particles within DTX–BSA droplets to 185 nm UV induced electrostatic interactions and the formation of Au₁Ag₉@DTX–BSA NBs, which were identified through the rearrangement of lattice spacings (Figure S3). Increased spacings may be attributable to the incorporation of other components of DTX–BSA into Au₁Ag₉ particles *via* photoinduced electrostatic interactions, reassembling the incorporation of Au₁Ag₉ particles into Au₁Ag₉@DTX–BSA NBs. Correspondingly, the Δ_{Ag} value for Ag 3d in Au–Ag@DTX–BSA, Au–Ag@DTX–BSA, and AuxAg @DTX–BSA NBs increased to 6.1 eV with distortion of the Ag 3d doublets,⁵⁹ while there were no distinguishable doublets (Δ_{Au}) for Au 4f in the NBs, probably because of the significantly reduced Au fraction (Figure S5). Analogous phenomena were observed in a previous study,⁶⁰ where incorporation of multiple components on sub-10 nm metallic particles significantly attenuated XPS signals of the small particles. This supports the incorporation of DTX–BSA components into the near-surface regions of Au₁Ag₉ particles (attenuating signals even in the case of Au with a higher work function) during passage through the photochamber. This reassembly was also confirmed by light absorbance of the NBs, including Au, Ag, and AuxAg particles, using UV–vis spectrophotometry (Figure 3B). Coexistence of Au and Ag atoms caused the light absorption spectra of both the Au and Ag particles to broaden³¹ probably due to pinhole formation in the NBs after electrostatic combination with DTX–BSA.⁶¹ Slight differences in absorption spectra were observed between the NBs, possibly because of the different levels of photoionization of the electrostatic interactions with DTX–BSA. The shoulder generation around at 350 nm may be related to the imbalanced collection (between Au and Ag) of the surface plasmon resonance.^{62–64} Loading capacities of the different NBs were elucidated (Figure S6) and found to be identical (~10%), suggesting that the single-pass fabrication can be

systemically optimized and controllable for loading DTX. The photothermal activity of Au–Ag@DTX–BSA, Au–Ag@DTX–BSA, and AuxAg@DTX–BSA NBs (Figure S7) was examined with four different NIR power densities (0.5, 1.0, 1.5, and 2.0 W/cm²). The photothermal conversion efficiencies of Au–Ag@DTX–BSA, Au–Ag@DTX–BSA, and AuxAg@DTX–BSA NBs after laser exposure were $34.6 \pm 2.2\%$, $38.1 \pm 1.4\%$, and $49.4 \pm 0.9\%$, respectively (Figure S8), which are comparable with the efficiencies of AuAg NP composites (<100 nm) in a previous study.⁷ For effective hyperthermia and disintegration, 2 W/cm² was selected as an optimal power density for this study. These conversion efficiencies of NBs induced the temperature elevations (Figure 3C and D), where the temperatures of NIR-exposed regions reached 40.3, 44.4, and 50.1 °C after 5 min of irradiation (808 nm, 2 W/cm²) for Au–Ag@DTX–BSA, Au–Ag@DTX–BSA, and AuxAg@DTX–BSA NBs, respectively. Interestingly, Au–Ag@DTX–BSA (remotely molten) exhibited greater temperature increases compared with Au–Ag@DTX–BSA (closely molten) from NIR exposure, which might be due to interparticle plasmonic coupling between individual Au and Ag particles that were in close proximity.^{65,66} Deformation of the NBs after 5 min of NIR irradiation was examined by TEM to evaluate renal excretion of Au₁Ag₉ particles through photothermal disintegration (Figure 3A). The high-magnification images (insets) clearly demonstrate the sizes of embedded Au–Ag (~6.0 nm), Au–Ag (~5.3 nm), or AuxAg (~5.2 nm) particles (dark dots represent single particles) in the block-like DTX–BSA upon photothermal collapse of the DTX–BSA matrix (soft dark flakes),^{67,68} which are within the appropriate size range (4–8 nm) for renal excretion. As shown in Figure S9, the plasmon-driven temperature increases after NIR irradiation^{69,70} led to the thermal degradation of peripheral BSA and subsequent disintegration of the NBs⁶⁸ probably because of higher local temperatures around Au₁Ag₉ particles than the lower critical solution temperature of BSA.⁷¹ In acidic pH (~5 for the repetitive NIR exposure in Figure S9), in addition, the disintegration might be accelerated due to repulsion between the positively charged Au₁Ag₉ particles.^{72,73} Dynamic light scattering (DLS, Figure S9) results after the four cycles of NIR irradiation supported the disintegration of the NBs, where the shift in size distribution was intensified from the repetitive irradiation. However, in the absence of NIR irradiation, there were no decreases in hydrodynamic particle size of the NBs (Figure S10) even in different media (phosphate-buffered saline [PBS], Dulbecco's modified Eagle's medium, and fetal bovine serum), supporting the critical role of NIR irradiation for NB disintegration. Thus, NIR-responsive collapse of the NBs may indicate eligibility for clearance from the body, therefore minimizing issues of deposition and toxicity of Au₁Ag₉ particles in the body.^{2,74} Figure 3E shows the photothermal conversion stability of the NBs from five on (5 min) and off (5 min) cycles; in particular, AuxAg@DTX–BSA NBs exhibited robust photothermal transduction despite photothermal disintegration, whereas the peak temperatures for the other two NBs decreased slightly, probably due to sintering phenomena in the near-surface regions of Au–Ag (aggravating crystalline perturbation) or Au–Ag (attenuating interparticle plasmonic coupling) particles upon repetitive NIR irradiation.⁷⁵ Nevertheless, NBs retained significant photothermal behavior because of no significant reshaping of Au₁Ag₉ particles after the repetitive NIR irradiation (refer to Figure S9),⁷⁶ suggesting that the plug-in manufacture system not only

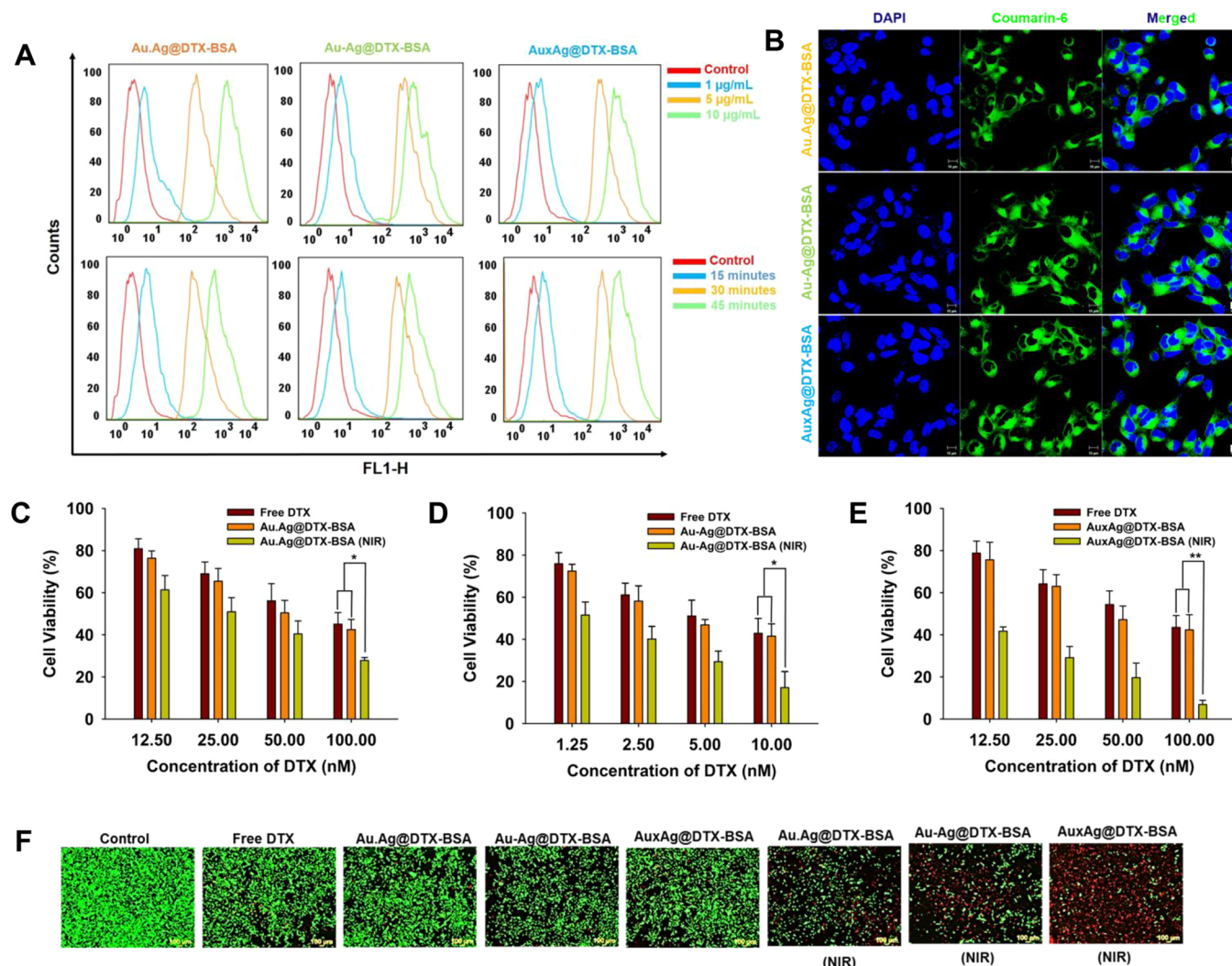


Figure 4. Intracellular uptake and cancer-cell-killing properties of Au₁Ag₉@DTX-BSA NBs. (A) Concentration (at 30 min)- and time (at 5 $\mu\text{g/mL}$)-dependent FACS profiles demonstrating cellular uptake of the three different NBs. (B) Representative confocal images of MDA-MB-231 cells treated with the three different NBs to assess NB localization. Coumarin-6 was used to stain the NBs, while DAPI was used to stain cell nuclei (scale bars, 10 μm). (C–E) Bar graphs illustrating the viability of the MDA-MB-231 cells treated with the three different NBs (at 12.5–100.0 $\mu\text{g/mL}$) for 24 h, including free DTX for comparison with or without NIR irradiation (808 nm, 2 W/cm², 5 min, N = 6). (F) Live/dead assay of MDA-MB-231 cells treated with identical configurations having an equivalent amount of DTX (5 nM) (scale bars, 100 μm).

provides photothermally modulatable modes but also offers stable photothermal transduction even over multiple NIR exposures. To examine the combinatorial chemotherapeutic effects of the NBs, we obtained time-dependent release profiles of DTX at different pH levels (7.4 [physiological] and 5.0 [endolysosomal]) and in the absence or presence of NIR irradiation (Figure 3F and G). Burst release of DTX was achieved at pH 5.0 in the presence of NIR,⁶⁹ suggesting stimulus functions of the NBs for site-selective release of DTX. Degradation of the BSA component in acidic and high-temperature conditions leads to disintegration of the DTX-BSA matrix and accelerated the release of DTX from the NBs. Irradiating with NIR thrice (5 min at predetermined time points) in acidic conditions can eliminate almost all embedded DTX (>96%) from the NBs in a short period of time, indicating the workability of NBs as phototriggered combinatorial chemotherapeutic agents in acidic cancer microenvironments.

The intracellular uptake of the three different NBs was examined using both fluorescence-activated cell sorting (FACS) and confocal laser scanning microscopy (CLSM). To obtain FACS profiles, different NB concentrations (1, 3, and 5 $\mu\text{g/mL}$) were subjected to a fixed exposure time (30 min), and a fixed NB concentration (3 $\mu\text{g/mL}$) was subjected to different exposure times (15, 30, and 45 min) to analyze uptake characteristics. The signals for NB uptake intensified with increasing NB concentration or exposure time, indicating that the NBs are internalized in a concentration- and time-dependent manner (Figure 4A). Following FACS analysis, the concentration and exposure time of 3 $\mu\text{g/mL}$ and 30 min, respectively, were selected for CLSM. Analysis of CLSM imaging revealed that coumarin-6-labeled NBs were distributed around the nucleus in the lysosome (Figures 4B and S11), reflecting the cellular internalization of NBs. *In vitro* cytotoxicity was assessed by 24 h incubation with 3-(4,5-dimethylthiazol-2-yl)-2,5-diphenyltetrazolium bromide (MTT) with or without NIR irradiation (Figure 4C–E). Cytotoxicity

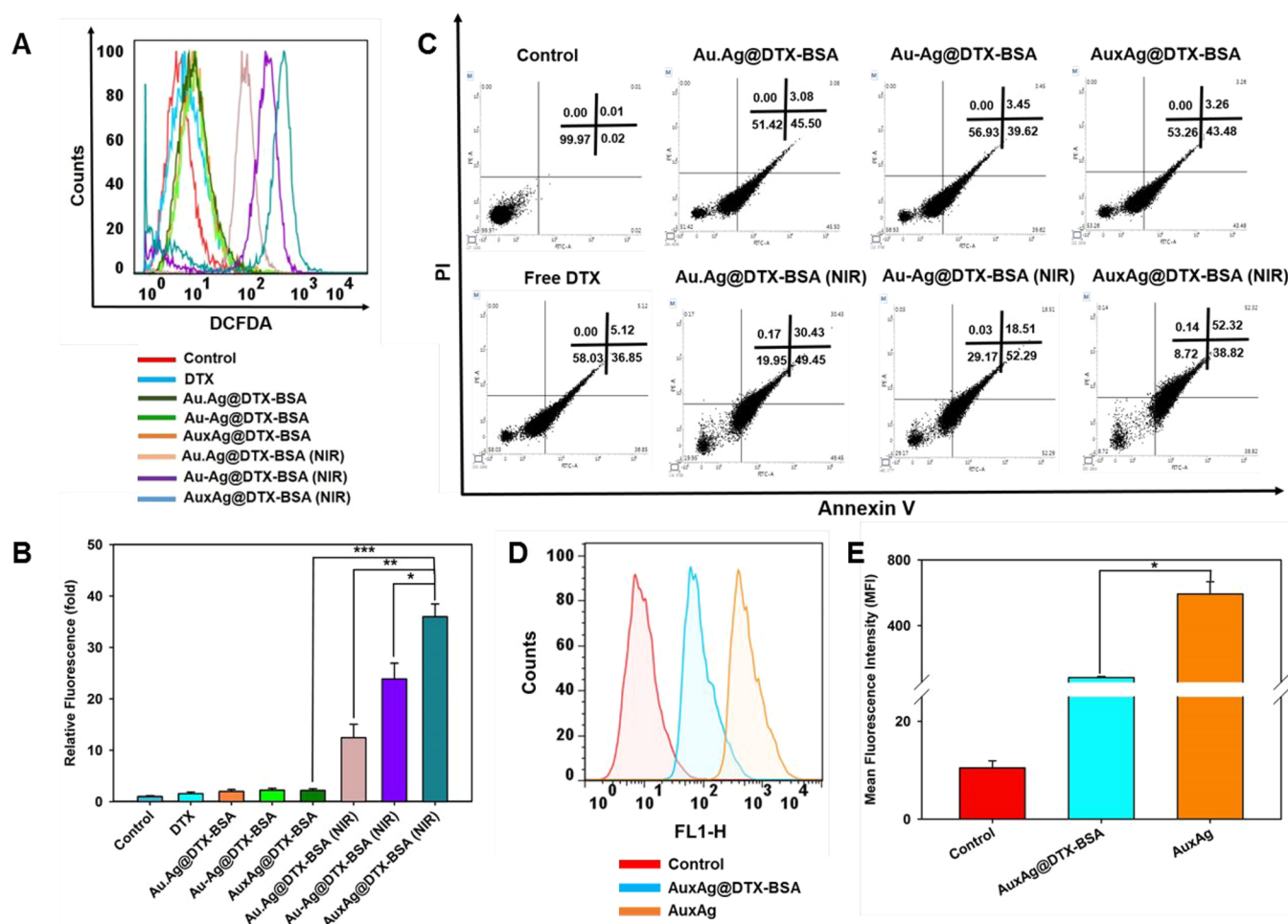


Figure 5. Generation of ROS and apoptosis following treatment with Au,Ag@DTX-BSA NBs and macrophage engulfment of AuxAg@DTX-BSA NBs. (A, B) FACS profiles and their quantified plots to measure ROS using DCFDA ($1 \mu\text{M}$) staining of MDA-MB-231 cells at 37°C for 1 h. Stained cells were treated with the three different NBs for 6 h, including free DTX for comparison, with or without NIR irradiation (808 nm , 2 W/cm^2 , 5 min , $N = 3$). (C) Bar graph of apoptosis results generated from identical treatments having an equivalent amount of DTX (5 nM). (D, E) Profiles and quantified plots of macrophage (RAW 264.7) uptake of AuxAg particles and AuxAg@DTX-BSA NBs after staining with fluorescein isothiocyanate ($1 \mu\text{g/mL}$), indicating the functions of BSA molecules ($N = 3$).

profiles of nonirradiated NBs were comparable with free DTX, whereas significantly greater cytotoxicity was observed following NIR irradiation. This demonstrates the combinatorial effects of heat and chemodrug for killing cancer cells. Because of the differences in photothermal transduction between the NBs, cytotoxicity profiles were as such: AuxAg@DTX-BSA > Au-Ag-DTX-BSA > Au-Ag@DTX-BSA, confirming the photothermally modulatable production. This is consistent with the images from the live/dead assay (Figures 4F and S12), which suggest the reproducibility of the modulatable property.

To clarify the combinatorial activity, reactive oxygen species (ROS) were assessed in NB-treated cells using flow cytometry, since excessive levels of intracellular ROS generally result in destruction of nucleic acids, proteins, membranes, and lipids, ultimately leading to activation of apoptosis.⁷⁷ As shown in Figure 5A and B, treatments with irradiated NBs significantly promoted ROS generation in cells, in line with the results from the MTT and live/dead assays. According to a previous study, the plasmon-driven production of radicals (e.g., $^1\text{O}_2$, $\text{O}_2^{\cdot-}$, and $^{\cdot}\text{OH}$), including hot electrons under laser irradiation, may induce the ROS generation in NB-treated cells.⁷⁸ DTX may

also be responsible for the ROS generation in which the generation was related to induction of the phosphorylation of protein kinase C β , as well as the promotion of nicotinamide adenine dinucleotide phosphate oxidase activity that results in mitochondrial dysfunction, endothelial apoptosis, and cell death.⁷⁹ Cellular apoptosis could also be up-regulated through mitochondrial depolarization and caspase protein stimulation by ROS production along with hyperthermia; therefore, an apoptosis assay was carried out. Flow cytometry profiles (Figure 5C) representing the fractions of live, early and late apoptotic, and necrotic cells show that treatments with NBs induced significantly greater fractions of early/late apoptotic cells than free DTX did. This effect was intensified following NIR irradiation because of the chemothermal effect, although there was still a negligible amount of necrotic cells, suggesting faster cell death occurs due to the chemothermal effect (i.e., curtailing the inflammatory responses because of the immediate action) compared with conventional radio- and chemotherapies, which induce coagulative necrosis. To make it vivid that the NIR laser itself is not responsible for the activity and does not induce any significant cytotoxicity, ROS generation, and apoptosis, the comparison to the laser-treated

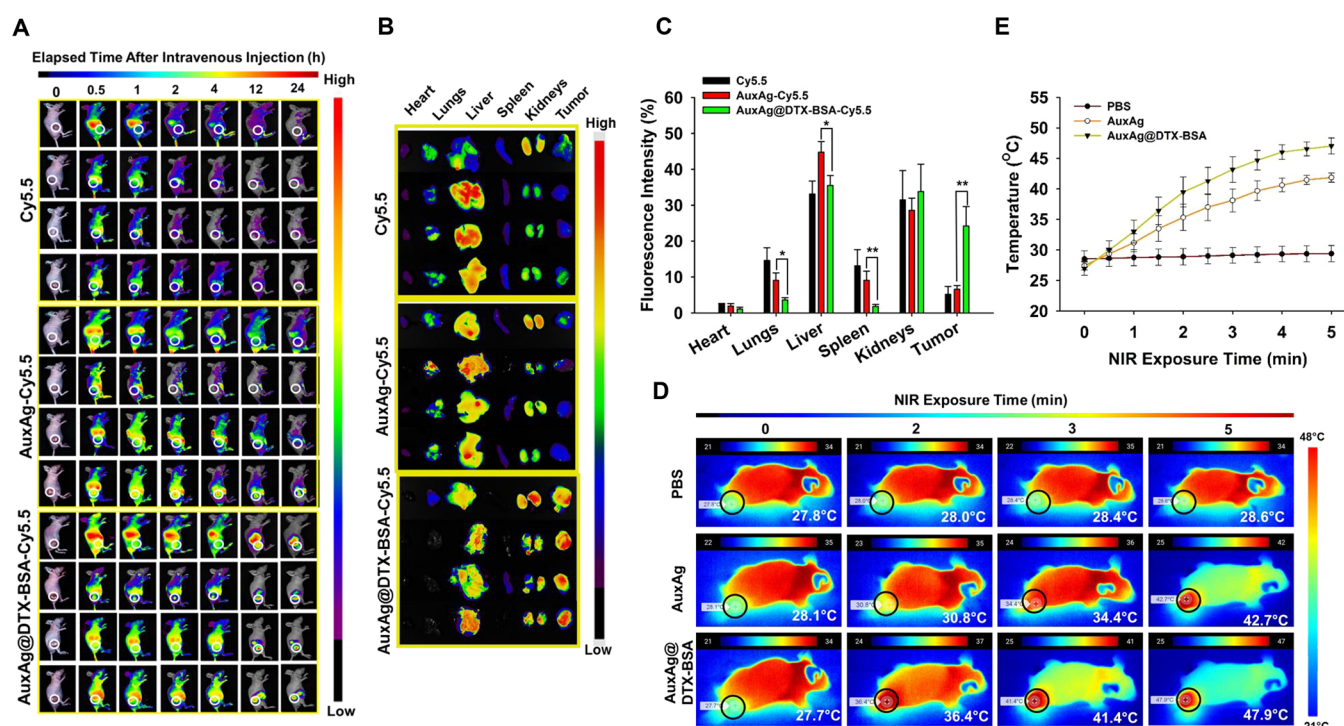


Figure 6. Biodistribution images of the *in vivo* tumor accumulation and photothermal activity of AuxAg@DTX-BSA NBs, including AuxAg particles for comparison. (A) Images of 24 h biodistribution profiles of Cy5.5-labeled AuxAg particles and AuxAg@DTX-BSA NBs in MDA-MB-231 xenograft mice after intravenous administration of particles. (B, C) *Ex vivo* imaging and quantified plots of Cy5.5-labeled AuxAg particles and AuxAg@DTX-BSA NBs in major organs and tumors 24 h after injection of particles, including free Cy5.5 for comparison (** $p < 0.01$, $N = 6$). (D, E) Photothermal contours and quantified plots following 5 min of NIR irradiation (808 nm, 2 W/cm², $N = 6$) of tumors after intravenous administration of particles. Xenografted tumor was exposed to NIR (circles in the images), and the temperatures in the tumor are specified in the lower right corner.

and untreated group was done. Figure S13 exhibits that the NIR irradiation did not induce significant differences in cell viability, photodynamic activity, and apoptosis, while no cytotoxic effects of AuxAg alone on MDA-MB-231 cells were observed in the absence of NIR irradiation (Figure S14), confirming the selective cytotoxic effects of the irradiation for the combination anticancer therapy. As shown in Figure S5D and E, RAW 264.7 macrophages (as model phagocytes) were also used to compare cellular uptake of AuxAg particles and AuxAg@DTX-BSA NBs and thus assess the utility of BSA for enhancing blood circulation time, since opsonization of the NBs should be prevented for targeted delivery into cancer cells.⁸⁰ The uptake of NBs was significantly lower than particles, which may be because of the protein (in BSA) resistance,⁸¹ which confirms the stealth properties of the NBs. This was also examined through the uptake measurement of NBs in a coculture system of RAW 264.7 macrophages and MDA-MB-231 cells (Figure S15), exhibiting similar results to the uptake without the use of a coculture system.

Biodistribution images were obtained 24 h after tumor-bearing mice were treated with cyanine 5.5 (Cy5.5)-labeled AuxAg@DTX-BSA NBs in order to examine tumor accumulation, and the results were compared with treatment with Cy5.5-labeled AuxAg particles and free Cy5.5 (Figures 6A and S16). After 24 h of intravenous injection, only NB-treated mice exhibited intense Cy5.5 signals in tumor regions, supporting the importance of BSA for targeted delivery. No notable accumulation of NBs was observed in the tumor region until 12 h despite increasingly intense signals compared with other treatments at all time points. This may support the

prominent retention of NBs in the bloodstream with no significant opsonization. *Ex vivo* imaging and quantified fluorescence (Figure 6B and C) further supported the high accumulation of NBs, which can be ascribed to their prolonged circulation time. An accumulation of Cy5.5-labeled NBs in kidneys was also observed, which may be because of repulsion between the embedded Au₁Ag₉ particles in acidic pH^{72,73} that leads to the accumulation in kidneys. Acceleration of this disintegration by NIR irradiation at the tumor region may intensify preferential decomposition for renal clearance. Considering the biodistribution results, NIR irradiation (2 W/cm²) was applied to mice after 24 h of treatment with AuxAg@DTX-BSA NBs, where the NB-treated mice exhibited the highest temperature elevation (Figure 6D and E), which proves the accumulation in tumor regions. In addition, accumulation in the heart, spleen, and lungs was significantly lower in NB-treated mice, indicating the appropriate biosafety profile in terms of inhibited retention in vital organs. Furthermore, the urinary excretion of AuxAg particles from mice treated with NIR-irradiated NBs (after 24 h of intravenous injection to confirm photothermal disintegration of the NBs) was evaluated using TEM after 72 h of intravenous injection (Figure S17), since the clearance of inorganic NPs is also critical for the biosafety of composite nanomedicines. Dark dots in the TEM images reflect the morphology and size distribution of the particles in Figure 3A (AuxAg@DTX-BSA NBs after exposure to NIR), verifying that the architecture of NBs confers NIR-induced disintegration, deep tumor penetration, and subsequent clearance of embedded AuxAg particles (sub-8 nm) through the kidneys (Figure 6B).⁴⁶

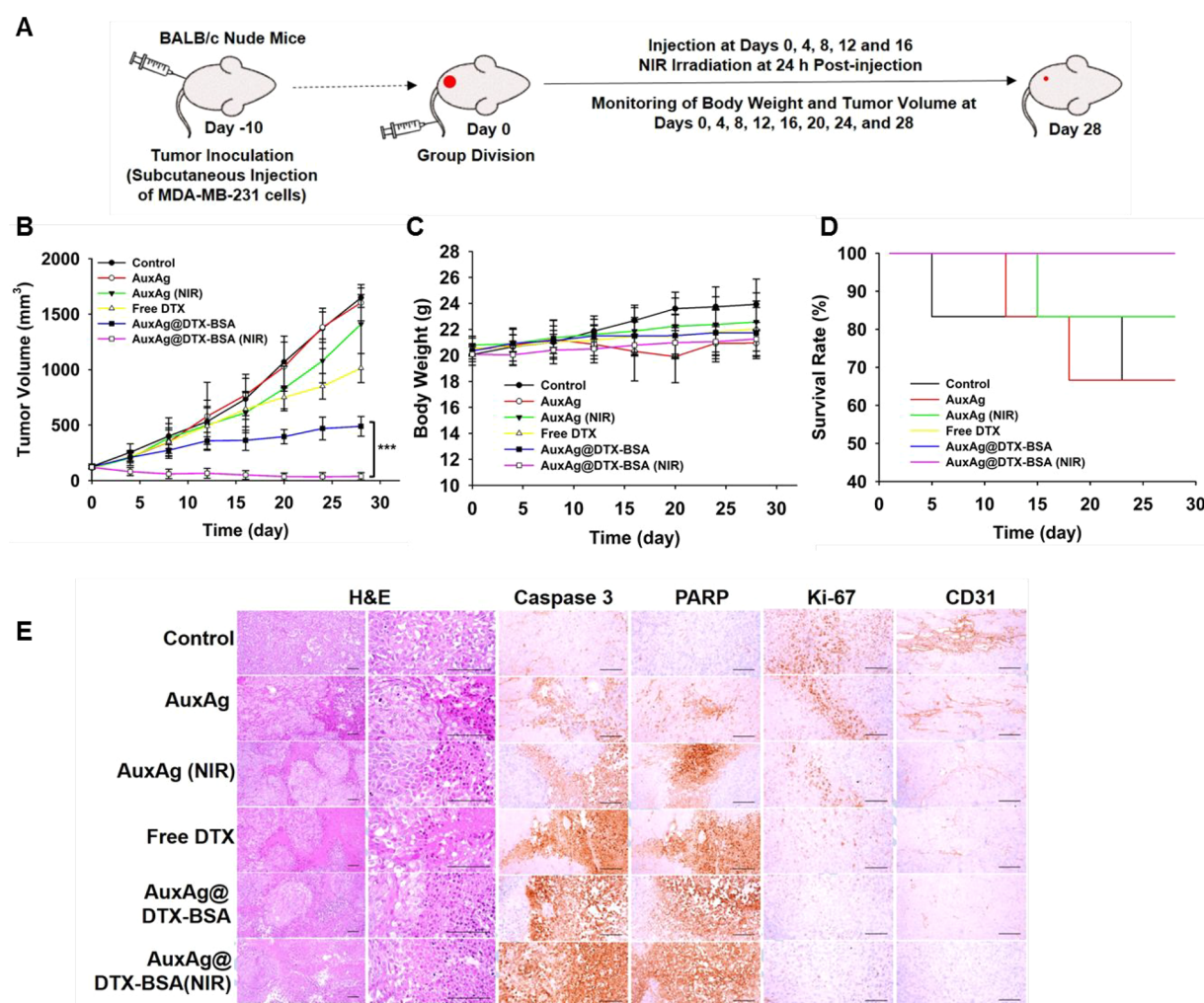


Figure 7. Illustration of the *in vivo* antitumor study using MDA-MB-231 xenograft BALB/c nude mice treated for 28 days. (A) Procedure of the antitumor study. (B–D) Time profiles of tumor volume, body weight, and survival rate of mice after treatment with AuxAg particles and AuxAg@DTX-BSA NBs with or without NIR irradiation (808 nm, 2 W/cm², 5 min, *N* = 6), including free DTX for comparison. (E) H&E and immunocytochemically stained (cleaved caspase-3, cleaved PARP, Ki-67, and CD31) tumor section images from identical treatments (scale bars, 120 μ m).

We performed *in vivo* antitumor analysis using the procedure depicted in Figure 7A to examine the systemic effects of AuxAg@DTX-BSA NBs in the absence and presence of NIR irradiation, as well as AuxAg particles and free DTX for comparison. There were no significant differences in tumor growth of the control (saline treatment) and AuxAg (without NIR)-treated groups, whereas NIR-irradiated AuxAg particles somewhat reduced the tumor growth rate because of the photothermal effect. However, the inhibitory rate of the latter was lower than that of free DTX. This implies that individual photodynamic or photothermal effect from NIR irradiation was not sufficient to be distinguished in the absence of other compounds. Combining AuxAg particles with DTX-BSA enhanced the inhibition of tumor growth, with significantly greater performance than free DTX even without NIR irradiation. This may be because of prolonged blood circulation ensuring tumor accumulation of NBs and thus providing targeted DTX release (the chemotherapeutic effect). The chemotherapeutic effect was strengthened with hyperthermia following NIR irradiation and further reduced the size of the original tumor (Figure 7B). Specifically, three of the six tumors were completely ablated after NB treatment with NIR

irradiation (Figure S18); thus, the weight of harvested tumors on the 28th day after this treatment was significantly lower than in other treatment groups (Figure S19) despite passive targeting and the fact that NIR cannot penetrate deeply through tissue. The body weight profile (Figure 7C) of the control group was increased due to tumor burden, whereas there were no significant alterations in other treatment groups, supporting the lack of systemic toxicities of the components of AuxAg@DTX-BSA NBs. The survival rates also clarified the biosafety profiles of the different treatments (Figure 7D). All mice treated with NBs in the absence and presence of NIR irradiation, including free DTX, remained alive throughout the study period (28 days). However, some mice of the control group died on the sixth and 24th day, and analogous events occurred in the AuxAg-treated group on the 13th and 19th day due to tumor burden. Tumor sections isolated from the different treatment groups were examined to evaluate cell apoptosis, angiogenesis, proliferation, and necrosis as critical biologic processes that are altered during treatments (Figure 7E). Apoptotic markers (cleaved caspase-3 and polyadenosine diphosphate-ribose polymerase [PARP]) were expressed in the following order: AuxAg@DTX-BSA (NIR) > AuxAg@

DTX-BSA > free DTX > AuxAg (NIR) > AuxAg, while markers of proliferation and angiogenesis (Ki-67 and CD31) were negatively correlated (Table S1), demonstrating the relationship between treatments and biological processes. The biosafety profiles of treatments were further examined through histopathological examination of the major organs (heart, liver, spleen, lung, and kidneys), as shown in Figure S20. No evident signs of toxicity were observed in the organs excised from mice, even those in the AuxAg treatment groups (no BSA was used to enhance blood circulation) (Table S2), highlighting the validity of embedding sub-8-nm AuxAg particles for renal excretion and minimization of toxicity from deposition and accumulation in the body. To examine the long-term biodistribution and fate of AuxAg particles *in vivo*, Au concentrations in the major organs of treated mice with AuxAg and AuxAg@DTX-BSA were monitored for 4 weeks using an inductively coupled plasma mass spectrometer (ICP-MS). The results exhibited that most Au in the organs of treated mice with AuxAg@DTX-BSA disappeared after 4 weeks, and the concentrations were significantly lower than those of treated mice with AuxAg (Figure S21), matching the results from the short-term biodistribution assay. This supports that embedding AuxAg particles in a DTX-BSA matrix is effective to avoid unwanted deposition of the particles on tissues of the organs. To confirm the acceleration of AuxAg clearance by NIR irradiation, Au concentrations in tumors, feces, and urine of the treated mice were also monitored. After 4 weeks, Au concentrations in tumors of the treated mice with AuxAg@DTX-BSA in the presence of NIR were significantly lower than those in feces and urine, as well as in tumors of the treated mice with AuxAg@DTX-BSA in the absence of NIR (Figure S22), reflecting NIR-induced disintegration of AuxAg@DTX-BSA for the clearance from the tumor. In detail, after 1 week of injection, NIR-treated groups exhibited about 2-fold greater clearance rate than the untreated ones. The Au concentrations in feces were comparable between the NIR-treated and untreated groups from 2 to 4 weeks after the injection, while there were constant 2-fold greater existences of Au in urine in the presence of NIR compared to untreated ones. This tendency may be ascribed to greater renal clearance of AuxAg particles in the presence of NIR, proving the NIR-responsive disintegration function of AuxAg@DTX-BSA. Nevertheless, the tumor localization and retention could be enhanced by incorporating targeting ligands; thus, further study is required to include a targeting agent in the plug-in system without sacrificing continuous fabrication. Modulating the ratio between Au and Ag, as well as applying different metals (e.g., other platinum group metals) also needs to be considered for future study to utilize minimal NIR laser power for safer treatments.

CONCLUSIONS

As a digitizable, continuous manufacture platform, heating plates (1336 °C), a spraying cup (2 L/min), and a photochamber (185 nm UV) were serially combined for plug-in continuous fabrication of Au-Au@DTX-BSA, Au-Ag@DTX-BSA, or AuxAg@DTX-BSA NBs under nitrogen gas flow. The three different AuAg particles were constructed before incorporating DTX-BSA molecules by changing the arrangement of molten Au and Ag disks on heating plates, where closely, remotely, and co-vaporized Au and Ag were condensed into sub-8-nm Au₁Ag₉, Au₁-Ag₉, and Au₁xAg₉ particles through nitrogen gas quenching. The Au₁Ag₉ particles

in all-in-one (Au₁Ag₉@DTX-BSA) droplets formed in the spraying cup were then positively charged through photon attack to facilitate surface electron ejection from the Au₁Ag₉ particles. This subsequently induced the incorporation of negatively charged groups from BSA into the positively charged particles, resulting in the formation of Au-Ag@DTX-BSA, Au-Ag@DTX-BSA, or AuxAg@DTX-BSA NBs after solvent extraction from the all-in-one droplets without any interruption of the flow reaction. Exposure of the NBs to NIR highlighted that the different arrangements for Au and Ag evaporation were able to modulate the photothermal effect of Au₁Ag₉ particles while maintaining disintegratable functions upon NIR exposure. Incorporation of DTX-BSA into Au₁Ag₉ particles (i.e., Au₁Ag₉@DTX-BSA NBs) significantly enhanced the cytotoxicity, ROS generation, and apoptotic alternation of the particles following NIR irradiation in response to effective intracellular uptake and successive DTX release. This led to enhanced tumor accumulation of the NBs and significant reduction in tumor size because of the chemothermal effects in the presence of NIR irradiation. Furthermore, disintegration of the NBs after NIR exposure indicated satisfactory biosafety profiles and the likelihood of renal excretion of Au₁Ag₉ particles. The strategy developed in this study not only provides an effective composite nanosystem for highly efficacious chemothermal cancer therapy but also describes a plug-in manufacture platform aiming toward automated or robotically realized fabrication of multimodal nanosystems for timely translation of nanosystems into various cancer treatments.

METHODS

Plug-in Manufacture of Au₁Ag₉@DTX-BSA NBs. As depicted in Figures 1 and S1A, plug-in reactionwares and the silicon nitride heating plate (SN220, Kyocera, Japan), spraying cup, and photochamber were connected in series to flow nitrogen gas (99.9999% purity) through the reactionwares in a single-pass manner. A variable-type direct current power supply (HCTm, South Korea), mass-flow controller (Tylan, USA), and UV lamp power supply (UVP, UK) were connected to the plate, cup, and chamber, respectively, to generate high temperatures (1336 °C), nitrogen flow (2 L/min), and UV radiation (185 nm wavelength). Equal generation of Au and Ag vapors was ensured using the different evaporation modes (Figure S1B; from closely [Au-Ag], remotely [Au-Ag], and co-molten [AuxAg] Au and Ag disks) by applying identical total weights of Au (AU-172561, Nilaco, Japan) and Ag (AG-402561, Nilaco) disks and flow rate of nitrogen. The imbalance between Au and Ag (1:9) vapors required to generate the Au₁Ag₉ configuration was achieved by using identical surface temperatures of the plates (1336 °C) directly applied to the Au and Ag disks, which have different melting points (Au: 1064.2 °C and Ag: 961.8 °C). Ambient nitrogen flow condensed the vapors into solid particles through nucleation–condensation, and this particle-laden flow was used as the main gas during operation of the spraying cup for the generation of DTX-BSA droplets. The Au₁Ag₉ particles floated in the nitrogen flow were merged with a DTX-BSA (3:1) solution (1 mg [DTX-BSA]/mL [ethanol]) near the orifice region of the cup due to gas pressurization; thus, all-in-one (Au₁Ag₉@DTX-BSA) droplets were continuously generated in the cup. These droplets were subsequently exposed to 185 nm UV (6.2 eV work function) during passage through the photochamber, where photons ejected electrons from Au₁Ag₉ particles (4.34 eV work function) to make the particles positively charged and thus facilitate electrostatic interaction between the particles and negative charged groups of BSA. This photoreaction-derived intervention inside the droplets led to the formation of block-shaped Au₁Ag₉@DTX-BSA after solvent extraction was carried out by passing through a diffusion dryer while in the aerosol state. By applying different evaporation modes,

Au-Ag@DTX-BSA, Au-Ag@DTX-BSA, and AuxAg@DTX-BSA NBs were harvested and dispersed in buffered saline for use in both *in vitro* and *in vivo* models.

Aerosol Size Distribution and Particle Charge. To confirm the incorporation of Au₁Ag₉ particles into DTX-BSA droplets, the aerosol size distributions of Au₁Ag₉ particles in the absence and presence of DTX-BSA were evaluated using an SMPS system (3936, TSI, USA) prior to passing through the diffusion dryer for solvent extraction. The SMPS consisted of a soft X-ray charge neutralizer (4530, HCT), DMA (3081, TSI), and condensation particle counter (3776, TSI). The hydrodynamic particle size distribution was analyzed using a DLS measurement system (Nano-S90, Malvern Instruments, UK).

To examine the positive charges and charge differences between Au₁Ag₉ and individual (pure Au and Ag) particles, an NDMA (3085, TSI) was placed before the photochamber to electrostatically classify the size of the particles (6 nm of equivalent mobility diameter) and enable relevant comparison between the particles. The electric current of size-classified particles was obtained using an aerosol electrometer (Charme, Palas GmbH, Germany).

Morphology, Composition, and Electronic State. The morphologies of Au₁Ag₉ particles and Au₁Ag₉@DTX-BSA NBs were analyzed by depositing particles on a carbon-coated copper grid (TedPella, USA) using a mini particle sampler (Ecomasure, France) with a vacuum pump (3033, TSI). The particle-deposited grid was transferred to a holder for TEM (Tecnai G2 F20 S-TWIN, FEI, USA) observation. Elemental composition of the Au₁Ag₉ particles was examined using an SEM-EDX system (S-4800, Hitachi, Japan) after deposition on a silicon substrate and subsequent sintering to ensure good particle distribution of Au and Ag and the immobilization of bigger particles for analytical clarity. Differences in the electronic state of Au₁Ag₉ particles and Au₁Ag₉@DTX-BSA NBs were examined using XPS (K-Alpha, Thermo Fisher Scientific, USA). To perform this, particles were collected on a polytetrafluoroethylene membrane filter (11807-47-N, Sartorius, Germany) *via* mechanical filtration. The elemental composition of Au₁Ag₉ particles was analyzed using XPS and compared with SEM-EDX observations.

Photothermal Effect. The NIR-induced photothermal effect of Au₁Ag₉@DTX-BSA NBs was monitored by acquiring temperature contour images with a digital thermal camera (Therm-App, Israel) at a distance of 7.5 cm between the NB dispersion (in PBS) and the NIR laser (808 nm laser; Changchun New Industries, China) with different power densities for optimization. After optimization, the dispersion concentration of NBs and laser power density were 25 $\mu\text{g/mL}$ and 2 W/cm^2 , respectively. The photothermal conversion efficiencies were calculated with the following equation:^{82,83}

$$\eta = (c_w m_w + c_n m_n) \Delta T / I A \Delta t \approx \eta = c_w m_w \Delta T / I A \Delta t$$

where c_w and m_w are the specific heat and mass of water, respectively, c_n and m_n are the analogous values of NBs, respectively. The ΔT is the elevated temperature after the time interval (Δt) of 5 min to reach thermal equilibrium. I and A are the NIR laser power intensity (2 W/cm^2) and exposed area to the laser beam (0.4 cm^2), respectively.

In Vitro DTX Release and Loading Capacity. Time profiles of DTX release from Au₁Ag₉@DTX-BSA NBs were obtained in different media, ABS (pH 5.0) and PBS (pH 7.4). The NB dispersion was injected into a dialysis bag (MWCO = 3500 Da; Spectrum Laboratories, USA), and the bag was subsequently immersed in a 50 mL tube containing 25 mL of acetate-buffered saline (ABS) or PBS. The tube was then incubated in a water bath shaker (Hanbaek ST Co., South Korea) at 100 rpm, 37 $^{\circ}\text{C}$. The amount released from the NBs was measured at predetermined time intervals using high-performance liquid chromatography (HPLC; 1260 Infinity II; Agilent Technologies, USA) with a C18 reversed-phase column (GL Sciences, Japan). Loading capacities of NBs were identified using HPLC.

Cytotoxicity. We seeded 1×10^4 MDA-MB-231 cells into each well of a 96-well plate and incubated the plate for 16 h to allow adhesion to the bottom of the wells. Cells were then treated with NBs for 24 h. For NIR irradiation, cells were exposed to NIR after 4 h of incubation with NBs and incubated for another 20 h. Treated cells

were washed twice with PBS and incubated for 4 h with 100 μL of MTT solution (1.25 mg/mL). Formazan crystals formed by live cells due to MTT metabolism were dissolved in 100 μL of dimethyl sulfoxide, and the absorbance was measured using a microplate reader (Thermo Scientific, USA) at 570 nm.

Cellular Uptake. The intracellular uptake of Au₁Ag₉@DTX-BSA NBs was determined using flow cytometry (BD FACS Calibur, BD Biosciences, USA) and visualized using CLSM (Leica Microsystems, Germany). For flow cytometry, 2×10^5 MDA-MB-231 cells were seeded into six-well plates and incubated for 20 h. These cells were treated with 3 $\mu\text{g/mL}$ of coumarin-6-loaded NBs for 15, 30, or 45 min (time-dependent analysis) or with 1, 5, or 10 $\mu\text{g/mL}$ of coumarin-6-loaded NBs for 30 min (concentration-dependent analysis). The treated cells were washed twice with PBS, trypsinized for collection, and suspended in 0.5 mL of PBS binding buffer for flow cytometry. For CLSM, 2×10^5 MDA-MB-231 cells were plated onto each coverslip of a six-well plate, incubated for 20 h, and treated with coumarin-6-loaded NBs for 30 min. After removal of culture media, the coverslips were washed gently twice with PBS, immobilized using 4% paraformaldehyde solution, attached to glass slides, and wrapped with glycerin. We used 4',6-diamidino-2-phenylindole (DAPI) stain to visualize cell nuclei, and the lysosome was stained using LysoTracker red.

Live/Dead Assay. We plated 2×10^5 MDA-MB-231 cells onto 12-well plates, incubated them for 16 h, and treated them with Au₁Ag₉@DTX-BSA NBs for 4 h with or without NIR irradiation. Treated cells were washed twice with PBS; then the media was replaced with fresh media and the plates were kept 10 cm beneath the rotating laser (2 W/cm^2 , 5 min) device. Cells were incubated for a further 20 h and washed twice with PBS, and the media were replaced with media containing calcein-acetoxymethyl (to observe live cells by green fluorescence) or ethidium homodimer (to observe cells by red fluorescence) for observation on an inverted fluorescence microscope (Eclipse Ti, Nikon, Japan).

Apoptosis. We seeded 2×10^5 MDA-MB-231 cells into a 12-well plate, incubated them for 12 h, and treated them with Au₁Ag₉@DTX-BSA NBs with or without NIR irradiation. After 48 h of treatment, cells were washed twice with PBS, trypsinized, resuspended in binding buffer containing PE-annexin-V and propidium iodide, incubated for 15 min in the dark, and suspended in binding buffer for flow cytometry.

ROS Generation. We treated 2×10^5 MDA-MB-231 cells with Au₁Ag₉@DTX-BSA NBs for 6 h with or without NIR irradiation and incubated them with 2',7'-dichlorofluorescein diacetate (DCFDA; green fluorescence) for 1 h. Treated cells were washed twice with PBS and trypsinized before harvesting for flow cytometry. Levels of ROS in the treated cells were determined by measuring green fluorescence.

Cellular Uptake into Macrophages. The Au₁Ag₉ particles and Au₁Ag₉@DTX-BSA NBs was assessed by incubating NBs with RAW 264.7 murine macrophage cells. Briefly, macrophages were incubated in 12-well plates and treated with the particles or NBs for 1 h. Coumarin-6 was used as a tag to determine the uptake levels by flow cytometry.

Biodistribution. We injected AuxAg particles or AuxAg@DTX-BSA NBs intravenously into MDA-MB-231 xenograft-bearing BALB/c nude mice after tagging Cy5.5 (1 $\mu\text{g/mL}$) onto the particles or NBs. Biodistribution was evaluated using the fluorescence-labeled organism bioimaging instrument system (Neoscience, South Korea). At 24 h after the injection, mice were placed in the imaging system, and Cy5.5 distributions monitored for 24 h. To perform *ex vivo* imaging, treated mice were sacrificed by carbon dioxide asphyxiation, and tumors and major organs were harvested. The tissues were placed in the imaging system, and fluorescence intensities were quantified using NEO imaging software.

In Vivo Photothermal Effect. After intravenous injection of AuxAg particles or AuxAg@DTX-BSA NBs, temperature contours were acquired using a digital thermal camera (Therm-App). Briefly, injected mice were incubated for 24 h; then tumors were irradiated with NIR radiation for 5 min and temperature contours simultaneously captured to examine the photothermal effects.

Histopathological Analysis. Major organs were excised from treated mice and sliced (3–4 μm), implanted in paraffin, and stained with hematoxylin and eosin (H&E) for observation using an optical microscope (Eclipse 80i, Nikon).

In Vivo Antitumor Study. After subcutaneous injection of 2×10^7 MDA-MB-231 cells, MDA-MB-231 xenograft tumors were developed in 5-week-old female BALB/c nude mice. Mice were distributed into six groups (six mice per group) when the tumors reached $\sim 100 \text{ mm}^3$ and were subsequently treated with AuxAg particles or AuxAg@DTX–BSA NBs with or without NIR irradiation (after 24 h of injection). Free DTX was injected for comparison at an equivalent dose (5 mg/kg). Tumor volumes were estimated using $1/2 \times \text{longest dimension} \times \text{shortest dimension}^2$. Dimensions were measured using vernier calipers.

Immunohistochemical Analysis. Tumor slices from treated mice were excised to assess the expression of apoptotic markers (cleaved caspase-3 and cleaved PARP), angiogenesis marker (CD31), and tumor cell proliferation marker (Ki-67). The assay was performed using a peroxidase substrate kit under incubation of purified primary antibodies with avidin–biotin–peroxidase complex. To obstruct endogenous peroxidase activity, the sections were treated in methanol and 0.3% hydrogen peroxide for 30 min. To inhibit nonspecific binding of immunoglobulin, the sections were incubated with horse serum blocking solution for 1 h in a humid chamber after heat treatment (95–100 $^{\circ}\text{C}$) based epitope retrievals in 10 mM citrate buffers (pH 6.0). After overnight treatment with antisera at 4 $^{\circ}\text{C}$, the sections were incubated with biotinylated secondary antibody and ABC reagent at room temperature for 1 h. The peroxidase substrate kit was eventually utilized to react with the sections for 3 min, and the sections were washed thrice with 0.01 M PBS. The expression levels of cleaved caspase-3, cleaved PARP, Ki-67, and CD31 in tumor cells were estimated using an automated image analyzer and presented as %/mass of tumor mass.

Biodistribution and Clearance Analysis. BALB/c nude mice were divided into 12 groups ($N = 3$), four groups were injected with AuxAg, while eight groups were injected with AuxAg@DTX–BSA (10 mg/kg of Au), and the tumor regions of the treated mice were exposed to NIR after 24 h of injection. For urine and feces collection, the mice were transferred to metabolic cages. The mice were then sacrificed, and the organs and tumors were harvested at each week after the injection. The tissues of hearts, livers, lungs, spleens, and kidneys, as well as urine and feces samples, were digested using a TOPEX microwave system (PreeKem, China) for ICP-MS quantitative analysis. The samples were digested with a mixture of aqua regia (5 mL) and deionized water (5 mL). The digestion solutions were finally diluted and analyzed on a NexION 300 ICP-MS system (PerkinElmer, USA).

All mouse experiments were approved and carried out in accordance with the instructions and guidelines of the Institutional Animal Ethics Committee, Yeungnam University, Republic of Korea.

ASSOCIATED CONTENT

Supporting Information

The Supporting Information is available free of charge at <https://pubs.acs.org/doi/10.1021/acsnano.9b09731>.

Additional information (PDF)

AUTHOR INFORMATION

Corresponding Authors

Jeong Hoon Byeon – School of Mechanical Engineering, Yeungnam University, Gyeongsan 38541, Republic of Korea; orcid.org/0000-0003-0903-7128; Email: postjb@yu.ac.kr

Jong Oh Kim – College of Pharmacy, Yeungnam University, Gyeongsan 38541, Republic of Korea; orcid.org/0000-0002-4929-851X; Email: jongohkim@yu.ac.kr

Jungho Hwang – School of Mechanical Engineering, Yonsei University, Seoul 03722, Republic of Korea; orcid.org/0000-0002-0304-7360; Email: hwangjh@yonsei.ac.kr

Authors

Kishwor Poudel – College of Pharmacy, Yeungnam University, Gyeongsan 38541, Republic of Korea

Sungjae Park – School of Mechanical Engineering, Yonsei University, Seoul 03722, Republic of Korea

Sae Kwang Ku – College of Korean Medicine, Daegu Haany University, Gyeongsan 38610, Republic of Korea

Chul Soon Yong – College of Pharmacy, Yeungnam University, Gyeongsan 38541, Republic of Korea

Complete contact information is available at: <https://pubs.acs.org/doi/10.1021/acsnano.9b09731>

Author Contributions

*K. Poudel and S. Park contributed equally to this work.

Notes

The authors declare no competing financial interest.

ACKNOWLEDGMENTS

This research was supported by Basic Science Research Program through the National Research Foundation of Korea (NRF) funded by the Ministry of Science, ICT and Future Planning (NRF-2018R1A2A1A05020683). This research was also supported by the NRF (2018R1A2A2-A05021143) grant funded by the Korean Government and the Medical Research Center Program (2015R1A5A2009124) through the NRF funded by MSIP.

REFERENCES

- (1) Zeng, L.; Pan, Y.; Wang, S.; Wang, X.; Zhao, X.; Ren, W.; Lu, G.; Wu, A. Raman Reporter-Coupled Ag_{core}@Au_{shell} Nanostars for *In Vivo* Improved Surface Enhanced Raman Scattering Imaging and Near-Infrared-Triggered Photothermal Therapy in Breast Cancers. *ACS Appl. Mater. Interfaces* **2015**, *7*, 16781–16791.
- (2) Jiang, T.; Song, J.; Zhang, W.; Wang, H.; Li, X.; Xia, R.; Zhu, L.; Xu, X. Au-Ag@Au Hollow Nanostructure with Enhanced Chemical Stability and Improved Photothermal Transduction Efficiency for Cancer Treatment. *ACS Appl. Mater. Interfaces* **2015**, *7*, 21985–21994.
- (3) Miclăuș, T.; Beer, C.; Chevallier, J.; Scavenius, C.; Bochenkov, V. E.; Enghild, J. J.; Sutherland, D. S. Dynamic Protein Coronas Revealed as a Modulator of Silver Nanoparticle Sulphidation *In Vitro*. *Nat. Commun.* **2016**, *7*, 11770.
- (4) Chakraborty, I.; Feliu, N.; Roy, S.; Dawson, K.; Parak, W. J. Protein-Mediated Shape Control of Silver Nanoparticles. *Bioconjugate Chem.* **2018**, *29*, 1261–1265.
- (5) Zhao, Y.; Zhao, J.; Shan, G.; Yan, D.; Chen, Y.; Liu, Y. SERS-Active Liposome@Ag/Au Nanocomposite for NIR Light-Driven Drug Release. *Colloids Surf., B* **2017**, *154*, 150–159.
- (6) Podila, R.; Chen, R.; Ke, P. C.; Brown, J. M.; Rao, A. M. Effects of Surface Functional Groups on the Formation of Nanoparticle-Protein Corona. *Appl. Phys. Lett.* **2012**, *101*, 263701.
- (7) Liu, Z.; Cheng, L.; Zhang, L.; Yang, Z.; Liu, Z.; Fang, J. Sub-100 nm Hollow Au-Ag Alloy Urchin-Shaped Nanostructure with Ultra-high Density of Nanotips for Photothermal Cancer Therapy. *Biomaterials* **2014**, *35*, 4099–4107.
- (8) Qi, G.; Zhang, Y.; Xu, S.; Li, C.; Wang, D.; Li, H.; Jin, Y. Nucleus and Mitochondria Targeting Theranostic Plasmonic Surface-Enhanced Raman Spectroscopy Nanoprobes as a Means for Revealing Molecular Stress Response Differences in Hyperthermia Cell Death between Cancerous and Normal Cells. *Anal. Chem.* **2018**, *90*, 13356–13364.

- (9) Wu, W.; Shen, J.; Banerjee, P.; Zhou, S. Water-Dispersible Multifunctional Hybrid Nanogels for Combined Curcumin and Photothermal Therapy. *Biomaterials* **2011**, *32*, 598–609.
- (10) Qin, Z.; Du, T.; Zheng, Y.; Luo, P.; Zhang, J.; Xie, M.; Zhang, Y.; Du, Y.; Yin, L.; Cui, D.; Lu, Q.; Lu, M.; Wang, X.; Jiang, H. Glutathione Induced Transformation of Partially Hollow Gold-Silver Nanocages for Cancer Diagnosis and Photothermal Therapy. *Small* **2019**, *15*, 1902755.
- (11) Durán, N.; Silveira, C. P.; Durán, M.; Martínez, D. S. Silver Nanoparticle Protein Corona and Toxicity: A Mini-Review. *J. Nanobiotechnol.* **2015**, *13*, 55.
- (12) Hao, M.; Kong, C.; Jiang, C.; Hou, R.; Zhao, X.; Li, J.; Wang, Y.; Gao, Y.; Zhang, H.; Yang, B.; Jiang, J. Polydopamine-Coated Au-Ag Nanoparticle-Guided Photothermal Colorectal Cancer Therapy Through Multiple Cell Death Pathways. *Acta Biomater.* **2019**, *83*, 414–424.
- (13) Mao, W.; Kim, H. S.; Son, Y. J.; Kim, S. R.; Yoo, H. S. Doxorubicin Encapsulated Clicked Gold Nanoparticle Clusters Exhibiting Tumor-Specific Disassembly for Enhanced Tumor Localization and Computerized Tomographic Imaging. *J. Controlled Release* **2018**, *269*, 52–62.
- (14) Zhao, X.; Qi, T.; Kong, C.; Hao, M.; Wang, Y.; Li, J.; Liu, B.; Gao, Y.; Jiang, J. Photothermal Exposure of Polydopamine-Coated Branched Au-Ag Nanoparticles Induces Cell Cycle Arrest, Apoptosis, and Autophagy in Human Bladder Cancer Cells. *Int. J. Nanomed.* **2018**, *13*, 6413–6428.
- (15) Dominguez-Medina, S.; McDonough, S.; Swanglap, P.; Landes, C. F.; Link, S. *In Situ* Measurement of Bovine Serum Albumin Interaction with Gold Nanospheres. *Langmuir* **2012**, *28*, 9131–9139.
- (16) Goodman, A. M.; Cao, Y.; Urban, C.; Neumann, O.; Ayala-Orozco, C.; Knight, M. W.; Joshi, A.; Nordlander, P.; Halas, N. J. The Surprising *In Vivo* Instability of Near-IR-Absorbing Hollow Au-Ag Nanoshells. *ACS Nano* **2014**, *8*, 3222–3231.
- (17) Noh, M. S.; Lee, S.; Kang, H.; Yang, J.-K.; Lee, H.; Hwang, D.; Lee, J. W.; Jeong, S.; Jang, Y.; Jun, B.-H.; Jeong, D. H.; Kim, S. K.; Lee, Y.-S.; Cho, M.-H. Target-Specific Near-IR Induced Drug Release and Photothermal Therapy with Accumulated Au/Ag Hollow Nanoshells on Pulmonary Cancer Cell Membranes. *Biomaterials* **2015**, *45*, 81–92.
- (18) Jang, H.; Kim, Y.-K.; Huh, H.; Min, D.-H. Facile Synthesis and Intraparticle Self-Catalytic Oxidation of Dextran-Coated Hollow Au-Ag Nanoshell and Its Application for Chemo-Therotherapy. *ACS Nano* **2014**, *8*, 467–475.
- (19) Davenport, A.; Tolwani, A. Citrate Anticoagulation for Continuous Renal Replacement Therapy (CRRT) in Patients with Acute Kidney Injury Admitted to the Intensive Care Unit. *Clin. Kidney J.* **2009**, *2*, 439–447.
- (20) Li, J.; Wang, W.; Zhao, L.; Rong, L.; Lan, S.; Sun, H.; Zhang, H.; Yang, B. Hydroquinone-Assisted Synthesis of Branched Au-Ag Nanoparticles with Polydopamine Coating as Highly Efficient Photothermal Agents. *ACS Appl. Mater. Interfaces* **2015**, *7*, 11613–11623.
- (21) Wang, L.; Chen, Y.; Lin, H. Y.; Hou, Y.-T.; Yang, L.-C.; Sun, A. Y.; Liu, J.-Y.; Chang, C.-W.; Wan, D. Near-IR-Absorbing Gold Nanoframes with Enhanced Physiological Stability and Improved Biocompatibility for *In Vivo* Biomedical Applications. *ACS Appl. Mater. Interfaces* **2017**, *9*, 3873–3884.
- (22) Chen, Z.; Zhang, L.; He, Y.; Li, Y. Sandwich-Type Au-PEI/DNA/PEI-Dexa Nanocomplex for Nucleus-Targeted Gene Delivery *In Vitro* and *In Vivo*. *ACS Appl. Mater. Interfaces* **2014**, *6*, 14196–14206.
- (23) Elbakry, A.; Zaky, A.; Liebl, R.; Rachel, R.; Goepferich, A.; Breunig, M. Layer-By-Layer Assembled Gold Nanoparticles for siRNA Delivery. *Nano Lett.* **2009**, *9*, 2059–2064.
- (24) Liu, Y.; Xu, M.; Chen, Q.; Guan, G.; Hu, W.; Zhao, X.; Qiao, M.; Hu, H.; Liang, Y.; Zhu, H.; Chen, D. Gold Nanorods/Mesoporous Silica-Based Nanocomposite as Theranostic Agents for Targeting Near-Infrared Imaging and Photothermal Therapy Induced with Laser. *Int. J. Nanomed.* **2015**, *10*, 4747–4761.
- (25) Gao, J.; Huang, X.; Liu, H.; Zan, F.; Ren, J. Colloidal Stability of Gold Nanoparticles Modified with Thiol Compounds: Bioconjugation and Application in Cancer Cell Imaging. *Langmuir* **2012**, *28*, 4464–4471.
- (26) Kitson, P. J.; Marie, G.; Francoia, J.-P.; Zaleskiy, S. S.; Sigerson, R. C.; Mathieson, J. S.; Cronin, L. Digitization of Multistep Organic Synthesis in Reactionware for On-Demand Pharmaceuticals. *Science* **2018**, *359*, 314–319.
- (27) Adamo, A.; Beingessner, R. L.; Behnam, M.; Chen, J.; Jamison, T. F.; Jensen, K. F.; Monbaliu, J.-C. M.; Myerson, A. S.; Revalor, E. M.; Snead, D. R.; Stelzer, T.; Weeranoppanant, N.; Wong, S. Y.; Zhang, P. On-Demand Continuous-Flow Production of Pharmaceuticals in a Compact, Reconfigurable System. *Science* **2016**, *352*, 61–67.
- (28) Morton, S. W.; Herlihy, K. P.; Shopsowitz, K. E.; Deng, Z. J.; Chu, K. S.; Bowerman, C. J.; DeSimone, J. M.; Hammond, P. T. Scalable Manufacture of Built-To-Order Nanomedicine: Spray-Assisted Layer-By-Layer Functionalization of PRINT Nanoparticles. *Adv. Mater.* **2013**, *25*, 4707–4713.
- (29) Coley, C. W.; Thomas, D. A., III; Lummiss, J. A. M.; Jaworski, J. N.; Breen, C. P.; Schultz, V.; Hart, T.; Fishman, J. S.; Rogers, L.; Gao, H.; Hicklin, R. W.; Plehiers, P. P.; Byington, J.; Piotti, J. S.; Green, W. H.; Hart, A. J.; Jamison, T. F.; Jensen, K. F. A Robotic Platform for Flow Synthesis of Organic Compounds Informed by AI Planning. *Science* **2019**, *365*, No. eaax1566.
- (30) Yu, Y.; Mok, B. Y. L.; Loh, X. J.; Tan, Y. N. Rational Design of Biomolecular Templates for Synthesizing Multifunctional Noble Metal Nanoclusters Toward Personalized Theranostic Applications. *Adv. Healthcare Mater.* **2016**, *5*, 1844–1859.
- (31) Feng, Y.; Wang, G.; Chang, Y.; Cheng, Y.; Sun, B.; Wang, L.; Chen, C.; Zhang, H. Electron Compensation Effect Suppressed Silver Ion Release and Contributed Safety of Au@Ag Core-Shell Nanoparticles. *Nano Lett.* **2019**, *19*, 4478–4489.
- (32) Fan, M.; Lai, F.-J.; Chou, H.-L.; Lu, W.-T.; Hwang, B.-J.; Brolo, A. G. Surface-Enhanced Raman Scattering (SERS) from Au:Ag Bimetallic Nanoparticles: The Effect of the Molecular Probe. *Chem. Sci.* **2013**, *4*, 509–515.
- (33) Riehemann, K.; Schneider, S. W.; Luger, T. A.; Godin, B.; Ferrari, M.; Fuchs, H. Nanomedicine-Challenge and Perspectives. *Angew. Chem., Int. Ed.* **2009**, *48*, 872–897.
- (34) Xu, X.; Isik, T.; Kundu, S.; Ortalan, V. Investigation of Laser-Induced Inter-Welding between Au and Ag Nanoparticles and the Plasmonic Properties of Welded Dimers. *Nanoscale* **2018**, *10*, 23050–23058.
- (35) Ong, Z. Y.; Chen, S.; Nabavi, E.; Regoutz, A.; Payne, D. J.; Elson, D. S.; Dexter, D. T.; Dunlop, I. E.; Porter, A. E. Multibranched Gold Nanoparticles with Intrinsic LAT-1 Targeting Capabilities for Selective Photothermal Therapy of Breast Cancer. *ACS Appl. Mater. Interfaces* **2017**, *9*, 39259–39270.
- (36) Dutta, D.; Chattopadhyay, A.; Ghosh, S. S. Cationic BSA Templated Au-Ag Bimetallic Nanoclusters as a Theranostic Gene Delivery Vector for HeLa Cancer Cells. *ACS Biomater. Sci. Eng.* **2016**, *2*, 2090–2098.
- (37) Ke, P. C.; Lin, S.; Parak, W. J.; Davis, T. P.; Caruso, F. A Decade of the Protein Corona. *ACS Nano* **2017**, *11*, 11773–11776.
- (38) Johnston, B. D.; Kreyling, W. G.; Pfeiffer, C.; Schäffler, M.; Sarioglu, H.; Ristig, S.; Hirn, S.; Haberl, N.; Thalhammer, S.; Hauck, S. M.; Semmler-Behnke, M.; Eppel, M.; Hühn, J.; Pino, P. D.; Parak, W. J. Colloidal Stability and Surface Chemistry Are Key Factors for the Composition of the Protein Corona of Inorganic Gold Nanoparticles. *Adv. Funct. Mater.* **2017**, *27*, 1701956.
- (39) Khandelia, R.; Jaiswal, A.; Ghosh, S. S.; Chattopadhyay, A. Gold Nanoparticle-Protein Agglomerates as Versatile Nanocarriers for Drug Delivery. *Small* **2013**, *9*, 3494–3505.
- (40) Kolosnjaj-Tabi, J.; Lartigue, L.; Javed, Y.; Luciani, N.; Pellegrino, T.; Wilhelm, C.; Alloyeau, D.; Gazeau, F. Biotransformations of Magnetic Nanoparticles in the Body. *Nano Today* **2016**, *11*, 280–284.
- (41) Sunoqrot, S.; Bugno, J.; Lantvit, D.; Burdette, J. E.; Hong, S. Prolonged Blood Circulation and Enhanced Tumor Accumulation of

Folate-Targeted Dendrimer-Polymer Hybrid Nanoparticles. *J. Controlled Release* **2014**, *191*, 115–122.

(42) Cabral, H.; Matsumoto, Y.; Mizuno, K.; Chen, Q.; Murakami, M.; Kimura, M.; Terada, Y.; Kano, M. R.; Miyazono, K.; Uesaka, M.; Nishiyama, N.; Kataoka, K. Accumulation of Sub-100 nm Polymeric Micelles in Poorly Permeable Tumours Depends on Size. *Nat. Nanotechnol.* **2011**, *6*, 815–823.

(43) Tong, X.; Wang, Z.; Sun, X.; Song, J.; Jacobson, O.; Niu, G.; Kiesewetter, D. O.; Chen, X. Size Dependent Kinetics of Gold Nanorods in EPR Mediated Tumor Delivery. *Theranostics* **2016**, *6*, 2039–2051.

(44) Li, H.-J.; Du, J.-Z.; Du, X.-J.; Xu, C.-F.; Sun, C.-Y.; Wang, H.-X.; Cao, Z.-T.; Yang, X.-Z.; Zhu, Y.-H.; Nie, S.; Wang, J. Stimuli-Responsive Clustered Nanoparticles for Improved Tumor Penetration and Therapeutic Efficacy. *Proc. Natl. Acad. Sci. U. S. A.* **2016**, *113*, 4164–4169.

(45) Yahia-Ammar, A.; Sierra, D.; Mérola, F.; Hildebrandt, N.; Guével, X. L. Self-Assembled Gold Nanoclusters for Bright Fluorescence Imaging and Enhanced Drug Delivery. *ACS Nano* **2016**, *10*, 2591–2599.

(46) Wang, Y.; Wang, F.; Shen, Y.; He, Q.; Guo, S. Tumor-Specific Disintegratable Nanohybrids Containing Ultrasmall Inorganic Nanoparticles: From Design and Improved Properties to Cancer Applications. *Mater. Horiz.* **2018**, *5*, 184–205.

(47) Luo, Z.; Zheng, K.; Xie, J. Engineering Ultrasmall Water-Soluble Gold and Silver Nanoclusters for Biomedical Applications. *Chem. Commun.* **2014**, *50*, 5143–5155.

(48) Chou, L. Y. T.; Zagorovsky, K.; Chan, W. C. W. DNA Assembly of Nanoparticle Superstructures for Controlled Biological Delivery and Elimination. *Nat. Nanotechnol.* **2014**, *9*, 148–155.

(49) Kim, J.; Lee, Y. M.; Kang, Y.; Kim, W. J. Tumor-Homing, Size-Tunable Clustered Nanoparticles for Anticancer Therapeutics. *ACS Nano* **2014**, *8*, 9358–9367.

(50) Byeon, J. H.; Roberts, J. T. Aerosol Based Fabrication of Thiol-Capped Gold Nanoparticles and Their Application for Gene Transfection. *Chem. Mater.* **2012**, *24*, 3544–3549.

(51) Poudel, B. K.; Doh, K.-O.; Byeon, J. H. Ag Photoionization-Induced Single-Pass Assembly of Ag₂S Nanodots in Flowing Thiol Droplets. *Green Chem.* **2018**, *20*, 978–983.

(52) Chaudhary, A.; Gupta, A.; Khan, S.; Nandi, C. K. Morphological Effect of Gold Nanoparticles on the Adsorption of Bovine Serum Albumin. *Phys. Chem. Chem. Phys.* **2014**, *16*, 20471–20482.

(53) Chen, Q.; Wang, X.; Wang, C.; Feng, L.; Li, Y.; Liu, Z. Drug-Induced Self-Assembly of Modified Albumins as Nano-Theranostics for Tumor-Targeted Combination Therapy. *ACS Nano* **2015**, *9*, 5223–5233.

(54) Blanco, E.; Shen, H.; Ferrari, M. Principles of Nanoparticle Design for Overcoming Biological Barriers to Drug Delivery. *Nat. Biotechnol.* **2015**, *33*, 941–951.

(55) Kannan, P.; John, S. A. Synthesis of Mercaptothiadiazole-Functionalized Gold Nanoparticles and Their Self-Assembly on Au Substrates. *Nanotechnology* **2008**, *19*, 085602.

(56) Chen, M.; Wang, D.; Liu, X. Direct Synthesis of Size-Tailored Bimetallic Ag/Au Nano-Spheres and Nano-Chains with Controllable Compositions by Laser Ablation of Silver Plate in H₂AuCl₄ Solution. *RSC Adv.* **2016**, *6*, 9549–9553.

(57) Ni, Y.; Kan, C.; He, L.; Zhu, X.; Jiang, M.; Shi, D. Alloyed Au-Ag Nanorods with Desired Plasmonic Properties and Stability in Harsh Environments. *Photonics Res.* **2019**, *7*, 558–565.

(58) Han, S. W.; Kim, Y.; Kim, K. Dodecanethiol-Derivatized Au/Ag Bimetallic Nanoparticles: TEM, UV/VIS, XPS, and FTIR Analysis. *J. Colloid Interface Sci.* **1998**, *208*, 272–278.

(59) Yi, Z.; Luo, J.; Tan, X.; Yi, Y.; Yao, W.; Kang, X.; Ye, X.; Zhu, W.; Duan, T.; Yi, Y.; Tang, Y. Mesoporous Gold Sponges: Electric Charge-Assisted Seed Mediated Synthesis and Application as Surface-Enhanced Raman Scattering Substrates. *Sci. Rep.* **2015**, *5*, 16137.

(60) Lim, J.; Hwang, J.; Byeon, J. H. Reconfigurable Plug-And-Play Assembly for the Continuous Production of Composite Anodes for Modulating Lithium Storage. *Chem. Eng. J.* **2019**, *364*, 485–492.

(61) Vongsavat, V.; Vittur, B. M.; Bryan, W. W.; Kim, J.-H.; Lee, T. R. Ultrasmall Hollow Gold-Silver Nanoshells with Extinctions Strongly Red-Shifted to the Near-Infrared. *ACS Appl. Mater. Interfaces* **2011**, *3*, 3616–3624.

(62) van der Linden, M.; van Bunningen, A. J.; Amidani, L.; Bransen, M.; Elnaggar, H.; Glatzel, P.; Meijerink, A.; de Groot, F. M. F. Single Au Atom Doping of Silver Nanoclusters. *ACS Nano* **2018**, *12*, 12751–12760.

(63) Misra, M.; Singh, N.; Gupta, R. K. Enhanced Visible-Light-Driven Photocatalytic Activity of Au@Ag Core-Shell Bimetallic Nanoparticles Immobilized on Electrospun TiO₂ Nanofibers for Degradation of Organic Compounds. *Catal. Sci. Technol.* **2017**, *7*, 570–580.

(64) Boote, B. W.; Byun, H.; Kim, J.-H. One-Pot Synthesis of Various Ag-Au Bimetallic Nanoparticles with Tunable Absorption Properties at Room Temperature. *Gold Bull.* **2013**, *46*, 185–193.

(65) Song, J.; Zhou, J.; Duan, H. Self-Assembled Plasmonic Vesicles of SERS-Encoded Amphiphilic Gold Nanoparticles for Cancer Cell Targeting and Traceable Intracellular Drug Delivery. *J. Am. Chem. Soc.* **2012**, *134*, 13458–13469.

(66) Song, J.; Yang, X.; Jacobson, O.; Lin, L.; Huang, P.; Niu, G.; Ma, Q.; Chen, X. Sequential Drug Release and Enhanced Photo-thermal and Photoacoustic Effect of Hybrid Reduced Graphene Oxide-Loaded Ultrasmall Gold Nanorod Vesicles for Cancer Therapy. *ACS Nano* **2015**, *9*, 9199–9209.

(67) Li, F.; Lu, J.; Kong, X.; Hyeon, T.; Ling, D. Dynamic Nanoparticle Assemblies for Biomedical Applications. *Adv. Mater.* **2017**, *29*, 1605897.

(68) Huang, P.; Lin, J.; Li, W.; Rong, P.; Wang, Z.; Wang, S.; Wang, X.; Sun, X.; Aronova, M.; Niu, G.; Leapman, R. D.; Nie, Z.; Chen, X. Biodegradable Gold Nanovesicles with an Ultrastrong Plasmonic Coupling Effect for Photoacoustic Imaging and Photothermal Therapy. *Angew. Chem., Int. Ed.* **2013**, *52*, 13958–13964.

(69) Guo, W.; Chen, J.; Liu, L.; Eltahan, A. S.; Rosato, N.; Yu, J.; Wang, D.; Chen, J.; Bottini, M.; Liang, X.-J. Laser-Induced Transformable BiS@HSA/DTX Multiple Nanorods for Photoacoustic/Computed Tomography Dual-Modal Imaging Guided Photothermal/Chemo Combinatorial Anticancer Therapy. *ACS Appl. Mater. Interfaces* **2018**, *10*, 41167–41177.

(70) Xu, H.; Kemiktarak, U.; Fan, J.; Ragole, S.; Lawall, J.; Taylor, J. M. Observation of Optomechanical Buckling Transitions. *Nat. Commun.* **2017**, *8*, 14481.

(71) Strozyk, M. S.; Chanana, M.; Pastoriza-Santos, I.; Pérez-Juste, J.; Liz-Marzán, L. M. Protein/Polymer-Based Dual-Responsive Gold Nanoparticles with pH-Dependent Thermal Sensitivity. *Adv. Funct. Mater.* **2012**, *22*, 1436–1444.

(72) Phan, H. T. M.; Bartelt-Hunt, S.; Rodenhausen, K. B.; Schubert, M.; Bartz, J. C. Investigation of Bovine Serum Albumin (BSA) Attachment onto Self-Assembled Monolayers (SAMs) Using Combinatorial Quartz Crystal Microbalance with Dissipation (QCM-D) and Spectroscopic Ellipsometry (SE). *PLoS One* **2015**, *10*, 141282.

(73) Estey, T.; Kang, J.; Schwendeman, S. P.; Carpenter, J. F. BSA Degradation under Acidic Conditions: A Model for Protein Instability During Release from PLGA Delivery Systems. *J. Pharm. Sci.* **2006**, *95*, 1626–1639.

(74) Guo, L.; Panderi, I.; Yan, D. D.; Szulak, K.; Li, Y.; Chen, Y.-T.; Ma, H.; Niesen, D. B.; Seeram, N.; Ahmed, A.; Yan, B.; Pantazatos, D.; Lu, W. A Comparative Study of Hollow Copper Sulfide Nanoparticles and Hollow Gold Nanospheres on Degradability and Toxicity. *ACS Nano* **2013**, *7*, 8780–8793.

(75) Lu, A.-H.; Zhang, X.-Q.; Sun, Q.; Zhang, Y.; Song, Q.; Schüth, F.; Chen, C.; Cheng, F. Precise Synthesis of Discrete and Dispersible Carbon-Protected Magnetic Nanoparticles for Efficient Magnetic Resonance Imaging and Photothermal Therapy. *Nano Res.* **2016**, *9*, 1460–1469.

- (76) Cassano, D.; Santi, M.; D'Autilia, F.; Mapanao, A. K.; Luin, S.; Voliani, V. Photothermal Effect by NIR-Responsive Excretable Ultrasmall-In-Nano Architectures. *Mater. Horiz.* **2019**, *6*, 531–537.
- (77) Redza-Dutordoir, M.; Averill-Bates, D. A. Activation of Apoptosis Signalling Pathways by Reactive Oxygen Species. *Biochim. Biophys. Acta, Mol. Cell Res.* **2016**, *1863*, 2977–2992.
- (78) Gao, L.; Liu, R.; Gao, F.; Wang, Y.; Jiang, X.; Gao, X. Plasmon-Mediated Generation of Reactive Oxygen Species from Near-Infrared Light Excited Gold Nanocages for Photodynamic Therapy. *ACS Nano* **2014**, *8*, 7260–7271.
- (79) Poudel, K.; Thapa, R. K.; Gautam, M.; Ou, W.; Soe, Z. C.; Gupta, B.; Ruttala, H. B.; Thuy, H. N.; Dai, P. C.; Jeong, J.-H.; Ku, S. K.; Choi, H.-G.; Yong, C. S.; Kim, J. O. Multifaceted NIR-Responsive Polymer-Peptide-Enveloped Drug-Loaded Copper Sulfide Nanoplat-form for Chemo-Phototherapy Against Highly Tumorigenic Prostate Cancer. *Nanomedicine* **2019**, *21*, 102042.
- (80) Mariam, J.; Sivakami, S.; Dongre, P. M. Albumin Corona on Nanoparticles-A Strategic Approach in Drug Delivery. *Drug Delivery* **2016**, *23*, 2668–2676.
- (81) Liu, X.; Chen, Y.; Li, H.; Huang, N.; Jin, Q.; Ren, K.; Ji, J. Enhanced Retention and Cellular Uptake of Nanoparticles in Tumors by Controlling Their Aggregation Behavior. *ACS Nano* **2013**, *7*, 6244–6257.
- (82) Emami, F.; Banstola, A.; Vatanara, A.; Lee, S.; Kim, J. O.; Jeong, J.-H.; Yook, S. Doxorubicin and Anti-PD-L1 Antibody Conjugated Gold Nanoparticles for Colorectal Cancer Photochemotherapy. *Mol. Pharmaceutics* **2019**, *16*, 1184–1199.
- (83) Zhang, H.; Chen, H.-J.; Du, X.; Wen, D. Photothermal Conversion Characteristics of Gold Nanoparticle Dispersions. *Sol. Energy* **2014**, *100*, 141–147.